



Bacteria solve the problem of crowding by moving slowly

O. J. Meacock^{1,2,3,5}, A. Doostmohammadi^{4,5}, K. R. Foster^{1,2}✉, J. M. Yeomans⁴✉ and W. M. Durham^{1,3}✉

Bacteria commonly live attached to surfaces in dense collectives containing billions of cells¹. While it is known that motility allows these groups to expand en masse into new territory^{2–5}, how bacteria collectively move across surfaces under such tightly packed conditions remains poorly understood. Here we combine experiments, cell tracking and individual-based modelling to study the pathogen *Pseudomonas aeruginosa* as it collectively migrates across surfaces using grappling-hook-like pili^{3,6,7}. We show that the fast-moving cells of a hyperpilated mutant are overtaken and outcompeted by the slower-moving wild type at high cell densities. Using theory developed to study liquid crystals^{8–13}, we demonstrate that this effect is mediated by the physics of topological defects, points where cells with different orientations meet one another. Our analyses reveal that when defects with topological charge $+1/2$ collide with one another, the fast-moving mutant cells rotate to point vertically and become trapped. By moving more slowly, wild-type cells avoid this trapping mechanism and generate collective behaviour that results in faster migration. In this way, the physics of liquid crystals explains how slow bacteria can outcompete faster cells in the race for new territory.

Bacteria generate collective motility on surfaces through a variety of mechanisms^{2–5,14}. While flagellar-based swimming in three dimensions is perhaps the best understood form of bacterial locomotion, swimming cells must be concentrated by orders of magnitude for collective behaviours to emerge, which are typically disrupted within minutes by oxygen depletion^{15,16}. In contrast, groups of bacteria can spontaneously generate collective motility when pulling themselves across two-dimensional surfaces using twitching motility, which is instead driven by grappling-hook-like appendages called type IV pili^{3,6,7}. Here we study the relationship between individual and collective twitching motility within large groups of the opportunistic pathogen *Pseudomonas aeruginosa*. We focus on movement in subsurface colonies sandwiched between agar and a coverslip (Fig. 1a), where movement is driven by pili, not flagella (Extended Data Fig. 1a,b), and where high-resolution time-lapse imaging can be used to follow individual cells as they collectively move along the glass surface. However, the phenomena we describe are not specific to this one assay. We also show that the key features are reproduced in classical bacterial colonies grown on the surface of agar (Fig. 1a–d, Extended Data Fig. 2 and Supplementary Video 1).

Recent microfluidic experiments have shown that deleting the *pilH* gene, which encodes a response regulator in the two-component

system that regulates twitching motility¹⁷, causes cells to move faster than wild-type (WT) cells¹⁸, probably because they express a larger number of pili¹⁷. To confirm that this increase in speed also occurs in subsurface colonies, we developed a cell-tracking algorithm to record the movement of thousands of individual cells within a single field of view (Methods and Supplementary Video 2). This revealed that individual $\Delta pilH$ cells move approximately twice as fast as WT cells in both densely packed collectives (Fig. 1e and Extended Data Fig. 3a) and at lower cell densities (Extended Data Fig. 3b). However, this difference in individual cell speed did not translate to how quickly colonies spread across the surface. While the faster motility of $\Delta pilH$ cells allowed them to initially spread outwards faster than WT cells, their expansion rate plateaued after four hours. In contrast, the expansion rate of WT colonies steadily increased over a period of approximately six hours, eventually reaching a value four times greater than that of $\Delta pilH$ colonies and ten times greater than that of colonies of the non-piliated $\Delta pilB$ strain (Fig. 1f,g and Supplementary Video 3). An increase in individual motility, therefore, did not translate successfully to an increase in collective motility.

Previous work has shown that strains that dominate the nutrient-rich edge of colonies can obtain a substantial growth advantage¹⁹. To investigate how this might affect the competitive ability of $\Delta pilH$ cells, we inoculated surficial colonies with equal proportions of $\Delta pilH$ and WT cells. This revealed that $\Delta pilH$ cells remained trapped in the nutrient-poor interior of the colony, while WT cells migrated outwards (Fig. 2a), allowing the latter to undergo approximately three more cell divisions over a 48 h period (Fig. 2b). We next analysed the dynamics of this competition in greater detail using subsurface colonies and automated image analysis to simultaneously measure colony expansion rate, cell packing fraction and genotypic composition (Fig. 2c–g, Supplementary Fig. 1, Supplementary Video 4 and Supplementary Methods). Consistent with their initial rapid expansion in monoculture colonies, $\Delta pilH$ cells initially outnumbered WT cells at the expanding edge of the colony (hereafter ‘the front’). However, once the front transitioned from loosely packed groups of cells to a confluent monolayer (Fig. 2e,g), the colony expansion rate rapidly increased from $0.75 \mu\text{m min}^{-1}$ to $5.0 \mu\text{m min}^{-1}$ (Fig. 2d) while the proportion of $\Delta pilH$ cells at the front fell sharply, dropping from 82% at 200 min to 3% at 350 min (Fig. 2f).

What could be responsible for this rapid decline of $\Delta pilH$ despite its faster individual movement? Direct observation of the colony monolayer at the same time as the precipitous decline of fast-moving $\Delta pilH$ cells suggested that $\Delta pilH$ cells lack the ability to

¹Department of Zoology, University of Oxford, Oxford, UK. ²Department of Biochemistry, University of Oxford, Oxford, UK. ³Department of Physics and Astronomy, University of Sheffield, Sheffield, UK. ⁴Niels Bohr Institute, University of Copenhagen, Copenhagen, Denmark. ⁵These authors contributed equally: O. J. Meacock, A. Doostmohammadi. ✉e-mail: kevin.foster@zoo.ox.ac.uk; julia.yeomans@physics.ox.ac.uk; w.m.durham@sheffield.ac.uk

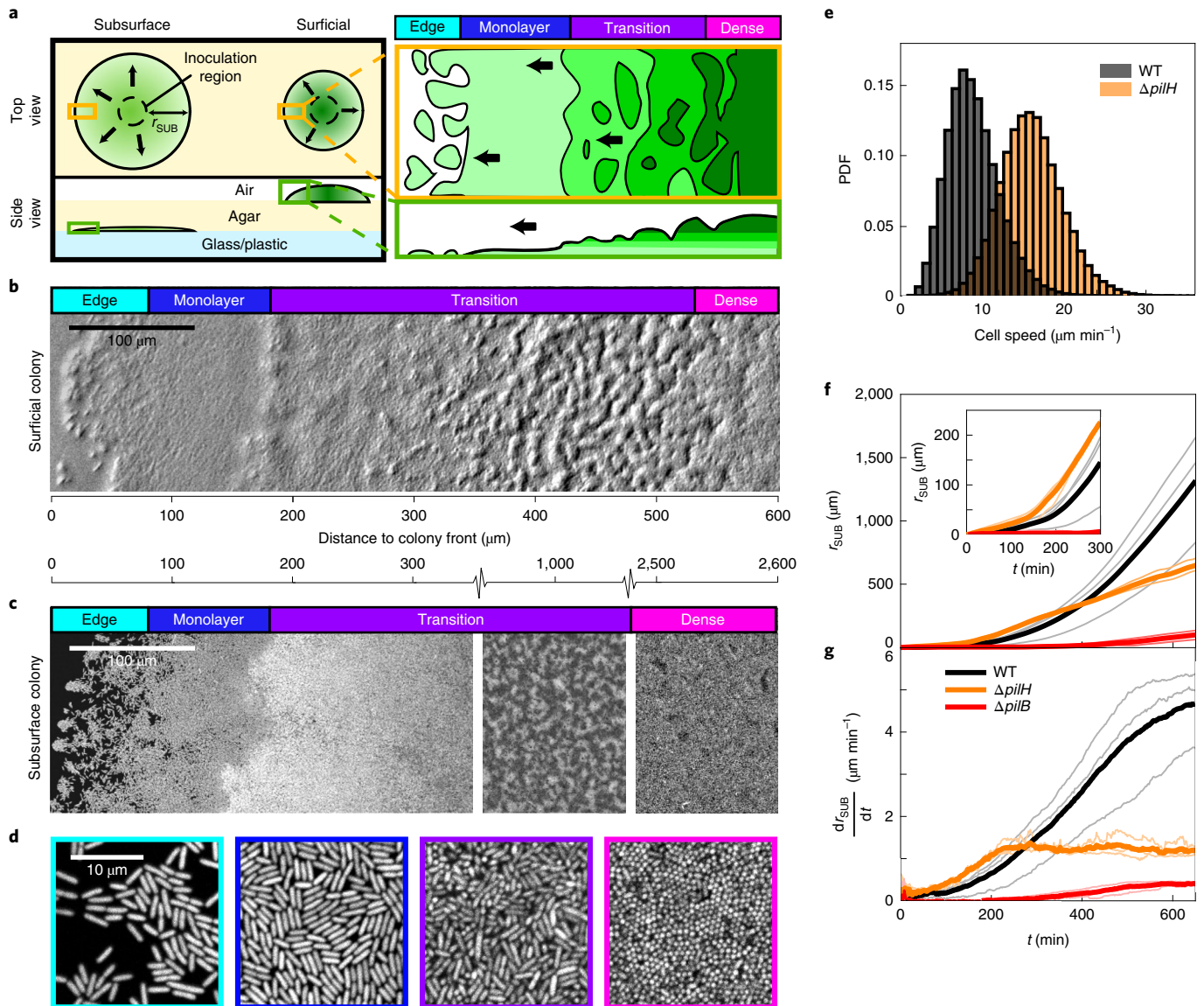


Fig. 1 | Pili-based motility drives the spread of *P. aeruginosa* colonies, but cells that individually move faster spread more slowly. **a**, Both subsurface colonies, which grow beneath a layer of agar, and surficial colonies, which grow on top of agar, consist of four distinct regions. **b,c**, In both surficial (**b**) and subsurface (**c**) WT colonies, the ‘edge’ contains small groups of loosely packed cells, the ‘monolayer’ is composed of tightly packed cells lying flat against the surface, the ‘transition’ region is a mixture of horizontally and vertically oriented cells, and in the ‘dense’ region almost all cells are vertical. **d**, Magnified views of each subsurface colony region. **e**, The probability density function (PDF) of the speed of individual WT and $\Delta pilH$ cells within the monolayer region. **f,g**, Measurements of the subsurface colony radius, r_{SUB} (**f**), and expansion rate, $\frac{dr_{SUB}}{dt}$ (**g**), for monocultures of WT (black), $\Delta pilH$ (orange) and non-piliated $\Delta pilB$ (red) cells. Inset in **f** shows a magnified view of the first 300 min. Panel **b** was imaged with oblique illumination microscopy; panels **c** and **d** were imaged with confocal microscopy. Bold lines in **f** and **g** indicate the mean of three separate experiments.

move collectively and were more likely to become trapped in place than WT cells (Supplementary Video 5). To understand how the collective behaviours of the two strains differ, we turned to tools originally developed to study liquid crystals. Densely packed cells tend to align in the same direction², and this nematic ordering produces collective movement on length scales substantially larger than that of a single cell^{20,21}. Moreover, we observed that topological defects, an emergent feature of nematic systems, move about within the monolayer of cells (Supplementary Video 6 and Methods). The two types of defects, with a topological charge of $+1/2$ and $-1/2$, respectively (Fig. 3a–c), denoted here as ‘comets’ and ‘trefoils’, are generated and annihilated in pairs (Extended Data Fig. 4a,b), as predicted by theory^{8,9}.

To investigate the physical properties of defects, we developed automated tools to combine single-cell-tracking data collected across hundreds of defects. This revealed that the movements of both WT cells (Fig. 3d) and $\Delta pilH$ cells (Extended Data Fig. 4c) around comets and trefoils closely match predictions from both an individual-based model of self-propelled rods (SPRs)¹⁵ and a continuum model of active nematics¹⁰, though $\Delta pilH$ flow fields are larger in scale than those of the WT. Theory predicts that comets migrate along their axis at a speed proportional to the activity of the nematic, a measure of the force exerted by each of the individuals that make up the system. In contrast, trefoils are predicted to move diffusively¹¹. Consistent with this, we observed that the root-mean-squared displacement (RMSD) of comets was larger in

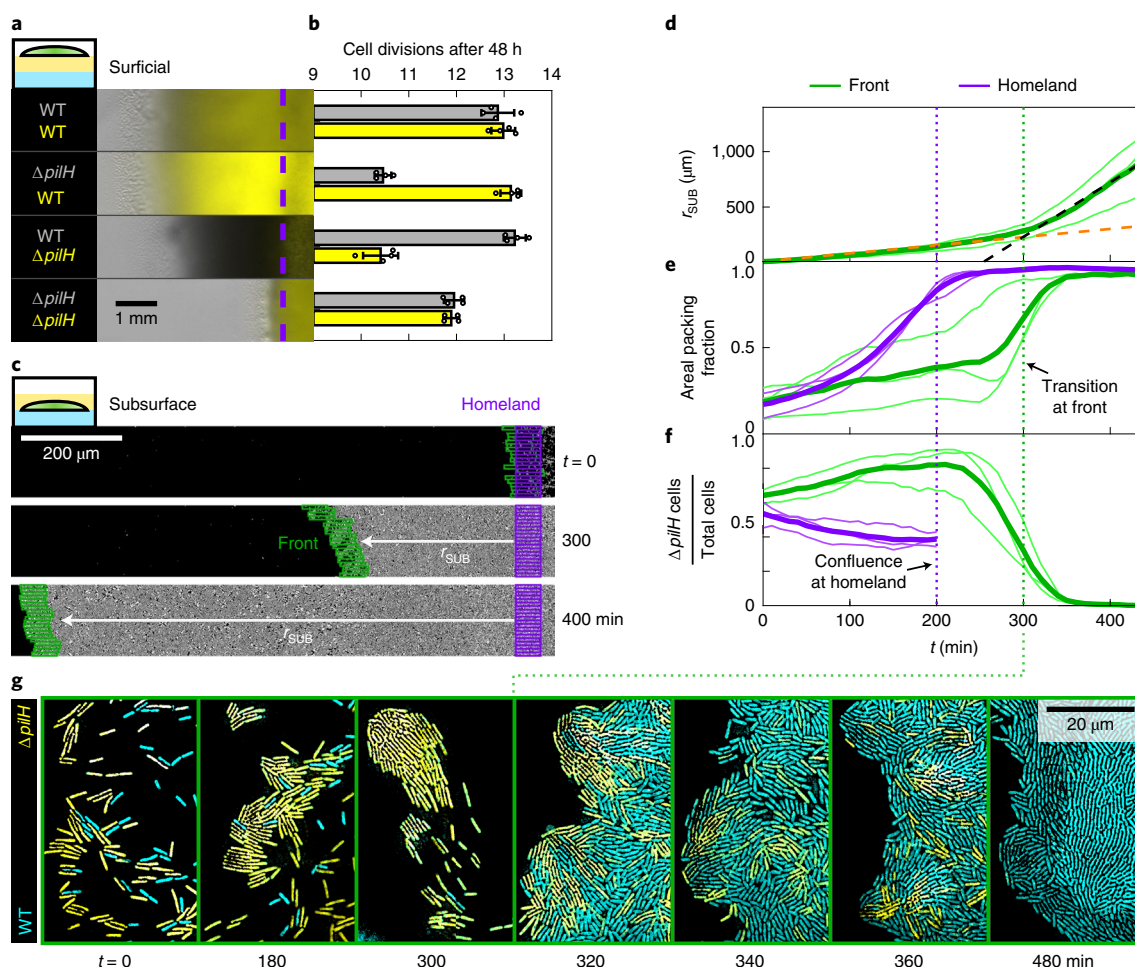


Fig. 2 | WT cells outcompete $\Delta pilH$ cells when mixed together in the same colony. **a**, Surficial colonies inoculated with equal proportions of YFP- and CFP-labelled cells after 48 h. Dashed purple lines indicate the boundary of the ‘homeland’, the region where cells are initially inoculated onto the agar. Due to imaging constraints (Methods), we show only the YFP and brightfield channels. Both strains appear in the latter, so regions with more CFP-labelled cells appear darker. **b**, Number of cell divisions occurring over 48 h of incubation within colonies shown in **a**. Grey and yellow bars denote populations labelled with CFP and YFP, respectively. Error bars show the standard deviation of four replicates. **c**, Subsurface colonies were initialized with equal proportions of YFP-labelled $\Delta pilH$ and CFP-labelled WT cells. We analysed dynamics within both the homeland (stationary, purple boxes) and the ‘front’ of the colony, which follows the edge of the colony as it expands (green boxes, Supplementary Video 4). **d**, Measurement of the distance between the front and homeland regions, r_{sub} , reveals a sevenfold increase in colony expansion rate at $t=300$ min (dashed lines, fitted with piecewise linear regression). **e, f**, The areal packing fraction (the fraction of the surface covered by cells) (**e**), and the relative frequency of $\Delta pilH$ cells (**f**) at the front also show sharp transitions at $t=300$ min. Bold lines in **d–f** indicate the mean from three separate experiments. Upon reaching confluence at $t=200$ min, cells in the homeland became too tightly packed to resolve their identity. **g**, Magnified images of the leading edge of a subsurface colony initiated with equal fractions of WT (cyan) and $\Delta pilH$ (yellow) cells. These images were processed as described in Methods.

$\Delta pilH$ monolayers than in WT monolayers, while the RMSD of trefoils was similar in both genotypes (Fig. 3e,f). These observations indicate that both WT and $\Delta pilH$ monolayers behave as an active nematic, with the latter possessing greater activity.

Comets elastically repel one another in a nematic confined to two dimensions¹². However, previous theoretical predictions^{9,13} and experiments with liquid crystals¹³ have suggested that when the nematic is allowed to reorient out of the two-dimensional (2D) plane, two comets with topological charge $+1/2$ could merge together at a sufficiently small separation, forming a $+1$ defect and causing the cells within to ‘escape into the third dimension’ by standing up vertically. We hypothesized that this process could occur only if the merging comets generated sufficient force to overcome the repulsion between them, potentially explaining why only the higher activity $\Delta pilH$ cells become trapped in place. To test this possibility, we first extended our SPR model to three

dimensions to allow rods to reorient out of the plane and simulated collisions between comets (Methods). Stable structures of upright rods (‘rosettes’) formed once the rods’ propulsive force, F , increased beyond a critical threshold, F_c , confirming our intuition (Fig. 4a, Extended Data Fig. 5, and Supplementary Videos 7 and 8). $\Delta pilH$ cells are also slightly longer than WT cells (Extended Data Fig. 6a), but this acts to suppress the nucleation of rosettes rather than promote it²² (Extended Data Fig. 6b–e and Supplementary Notes). To test whether the increased force generated by $\Delta pilH$ cells is alone sufficient to preferentially trap them in rosettes, we next used our 3D SPR model to simulate the interaction of two different genotypes that each exert a different propulsive force (Fig. 4b,c). This showed that higher-force mutants, on average, move more slowly than the WT cells because a larger fraction of the higher-force mutants become stuck in rosettes where their movement is arrested.

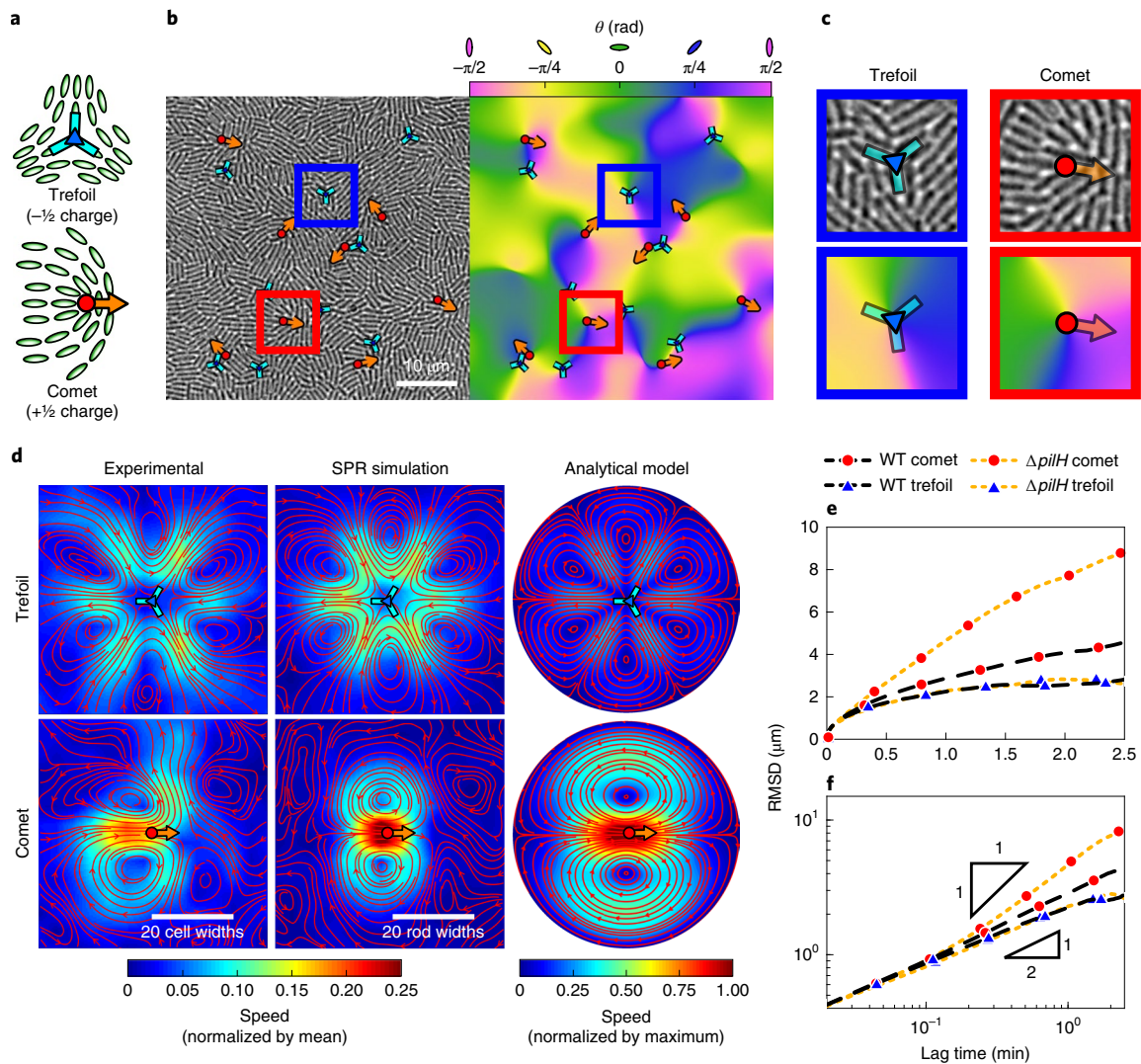


Fig. 3 | Subsurface colonies exhibit patterns of collective motility consistent with a nematic system driven out of equilibrium. **a**, Two types of topological defects occur in 2D nematic systems: trefoils, which show three-fold rotational symmetry and have a topological charge of $-1/2$, and comets, which migrate along their single axis of symmetry and have a charge of $+1/2$ (see text). **b**, The locations and orientations of defects in the monolayer of a WT subsurface colony (left, Supplementary Video 6) were obtained by quantifying the local cell orientation (right). **c**, Magnified views of the red and blue boxes in **b** illustrate how defects occur at singularities in cell orientation. **d**, Simultaneous tracking of both defects and individual cells within a monolayer (Supplementary Videos 2 and 6) allows the mean cell flow around defects to be resolved. The structure of the flow closely resembles that predicted from an SPR simulation and an analytical model (Methods and Supplementary Methods). Red lines show streamlines and the background colours indicate flow speed. **e, f**, The RMSD measures how far defects move over a given lag time, plotted here on both a linear (**e**) and a logarithmic (**f**) scale. Triangles in **f** show the slopes predicted for ballistic (1:1) and diffusive (1:2) movement.

We tested these theoretical predictions by inoculating subsurface colonies composed of a mixture of both $\Delta pilH$ and WT cells. In these colonies, we observed that $\Delta pilH$ cells spontaneously formed rosettes, whereas WT cells did not (Supplementary Video 5). Moreover, we were able to quantify the movement of topological defects when the fraction of $\Delta pilH$ cells in the front begins to sharply decrease (Fig. 2f). We observed comets approaching each other (Fig. 4d) before the monolayer of cells began to reorient out of plane, forming a rosette with a stable topological charge of $+1$ (Fig. 4e, Extended Data Fig. 7 and Supplementary Video 9) as predicted by our SPR model (Fig. 4a). Even though this colony was initiated with an equal fraction of WT and $\Delta pilH$ cells, confocal imaging revealed that the core of this rosette was nearly entirely composed of vertically oriented $\Delta pilH$ cells (Fig. 4f). Once initiated, rosettes in both experiments and simulations grew larger in size (Supplementary Videos 8 and 9). These dynamics are reminiscent of

the ‘inverse domino’ cascade of cell verticalization seen at the centre of non-motile *Vibrio cholerae* bacterial colonies when they reach a critical size^{22,23}, which is instead driven by buckling induced by cell division²².

The direct observation of rosettes in our experiments and their close correspondence with those observed in our models provides strong evidence that $\Delta pilH$ cells become trapped as a direct consequence of their higher activity. However, we also considered other possible pleiotropic effects of this mutation, such as an increase in doubling times²⁴ and cell–cell adhesion^{24,25}. Extensive analyses rule these out as explanations of the sudden decline of the fraction of $\Delta pilH$ cells at the colony front (Supplementary Notes and Extended Data Figs. 8 and 9). We also considered whether a deficiency in chemotaxis might play a role in the slower expansion of $\Delta pilH$ cells. We could not directly confirm, however, whether chemotaxis plays any role in colony expansion in our assays because the only known

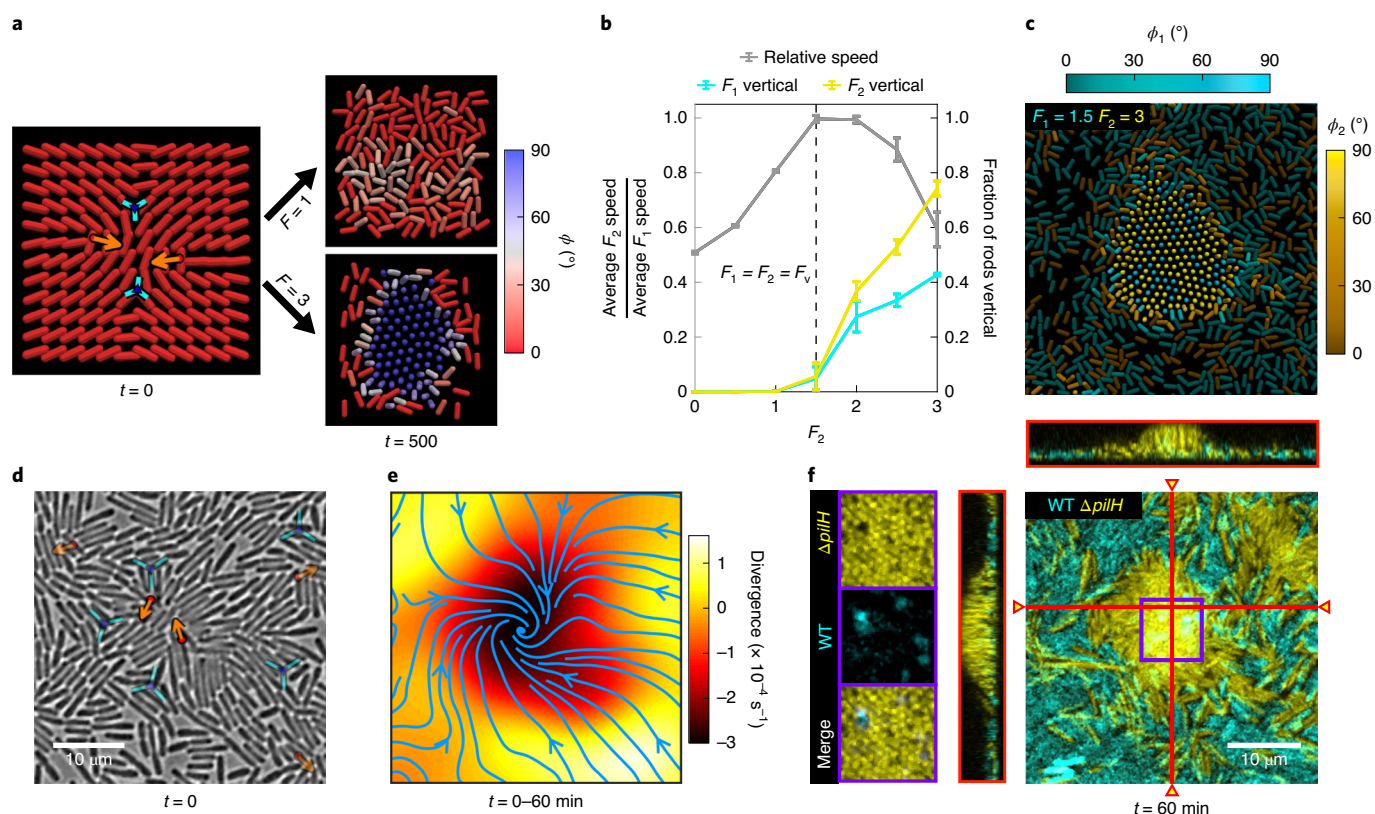


Fig. 4 | $\Delta pilH$ cells are preferentially trapped by rosettes, preventing their outward migration. **a**, A 3D SPR simulation of two comets colliding with one another shows that rods propelled by a smaller force ($F=1$) remain flat against the surface after an initial transient, while those propelled by a larger force ($F=3$) form a stable, vertically oriented rosette (Supplementary Video 7). Colour denotes the angle of rods relative to the surface, ϕ . **b**, SPR simulations initialized with randomly oriented rods, half of which are propelled by a fixed force of $F_1 = F_v = 1.5$ (cyan, 'WT') and the other half by a variable force F_2 (yellow, 'mutant'). The left axis shows the mean speed of the F_2 population at steady state normalized by that of the F_1 population. The right axis indicates the fraction of each population that is vertically oriented (defined as $\phi > 85^\circ$). Error bars indicate standard deviation of three different simulations, each with a different random initial configuration. **c**, A rosette from a $F_1 = 1.5$, $F_2 = 3$ simulation at steady state, where ϕ_1 and ϕ_2 denote the orientation of the two respective populations. **d**, Two comets approaching one another in a colony initiated with an equal number of WT and $\Delta pilH$ cells (Supplementary Video 9). **e**, Measurements of cell velocity within the same region as **d** during rosette development. Blue arrows and colourmap respectively show streamlines and divergence of the time-averaged flow field (Methods). Regions of negative divergence indicate zones of cell accumulation. **f**, Three-dimensional confocal image of the rosette that formed within the same region shown in **d** and **e**, taken 60 min after **d** (Methods). Vertical slices through the rosette are shown to the top and left, at locations indicated by triangles. Inset: a magnified view of the rosette (purple box in **f**) shows it is mostly composed of $\Delta pilH$ cells in a vertical orientation. Main panel shows maximal z-projection of both YFP and CFP channels, while insets show individual z slices.

mutant deficient in pili-based chemotaxis, $\Delta pilG^{18}$, shows little, if any, motility under agar (probably because they produce relatively few pili^{17,18}; Supplementary Notes and Extended Data Fig. 1c). We decided that a more straightforward and definitive test of whether rosette formation was responsible for $\Delta pilH$ cells' reduced capacity to spread was to cover colonies with progressively stiffer agar, which acts to increase the stabilizing torque that resists cell verticalization (Methods, equation (5)). Increasing the agar concentration of the overlying pad was observed to both dramatically suppress the formation of rosettes and allow $\Delta pilH$ cells to expand much farther before they were fully displaced by WT cells (for example, stiffer agar increased the proportion of $\Delta pilH$ cells in the front by 80-fold after 1.2 mm of collective expansion; Supplementary Notes and Extended Data Fig. 10). These experiments, along with the observations that the proportion of $\Delta pilH$ cells in the front only begins to decrease once cells transition from individual to collective motility and start to form rosettes (Fig. 2e,f and Supplementary Videos 5 and 9), strongly suggest that the loss of $\Delta pilH$ cells from the front of mixed colonies is caused primarily by their tendency to become trapped in rosettes, rather than due to a deficiency in chemotaxis or another putative mechanism.

Recently, two preliminary reports have shown that WT *P. aeruginosa* and *Myxococcus xanthus* cells can form multiple layers of horizontally aligned cells when moving collectively using pili-based motility^{26,27}. While we also observe that both WT and $\Delta pilH$ cells form these terrace-like structures at the very edge of our colonies (Extended Data Fig. 10c), their morphology and distribution is very different to the verticalized rosettes, which occur deeper within the colony and are dominated by the faster-moving $\Delta pilH$ cells. Nevertheless, these new studies contribute to our understanding of the diverse physical mechanisms that dictate the architecture of bacterial colonies and further illustrate how they can serve as model systems of active matter^{20,22,23,26–29}.

Our results show that the physics of active liquid crystals can exert a fundamental limit on the speed of motility within crowds of bacteria. Cells that exceed this critical threshold form high-velocity comets that are unstable to verticalization upon collision, causing fast-moving cells to become trapped within the interior of colonies where nutrients are scarce³⁰. However, bacteria that move more slowly as individuals are able to avoid this fate and collectively expand faster. In the race into new territory, the physical processes we describe therefore favour bacteria that exercise restraint by moving slowly and prudently.

Online content

Any methods, additional references, Nature Research reporting summaries, source data, extended data, supplementary information, acknowledgements, peer review information; details of author contributions and competing interests; and statements of data and code availability are available at <https://doi.org/10.1038/s41567-020-01070-6>.

Received: 14 July 2020; Accepted: 17 September 2020;

Published online: 23 November 2020

References

- Nadell, C. D., Drescher, K. & Foster, K. R. Spatial structure, cooperation and competition in biofilms. *Nat. Rev. Microbiol.* **14**, 589–600 (2016).
- Zhang, H. P., Beér, A., Florin, E.-L. & Swinney, H. L. Collective motion and density fluctuations in bacterial colonies. *Proc. Natl Acad. Sci. USA* **107**, 13626–13630 (2010).
- Gloag, E. S. et al. Self-organization of bacterial biofilms is facilitated by extracellular DNA. *Proc. Natl Acad. Sci. USA* **110**, 11541–11546 (2013).
- Wu, Y., Kaiser, A. D., Jiang, Y. & Alber, M. S. Periodic reversal of direction allows Myxobacteria to swarm. *Proc. Natl Acad. Sci. USA* **106**, 1222–1227 (2009).
- Shrivastava, A. et al. Cargo transport shapes the spatial organization of a microbial community. *Proc. Natl Acad. Sci. USA* **115**, 8633–8638 (2018).
- Talà, L., Fineberg, A., Kukura, P. & Persat, A. *Pseudomonas aeruginosa* orchestrates twitching motility by sequential control of type IV pili movements. *Nat. Microbiol.* **4**, 774–780 (2019).
- Skerker, J. M. & Berg, H. C. Direct observation of extension and retraction of type IV pili. *Proc. Natl Acad. Sci. USA* **98**, 6901–6904 (2001).
- Doostmohammadi, A., Ignés-Mullol, J., Yeomans, J. M. & Sagués, F. Active nematics. *Nat. Commun.* **9**, 3246 (2018).
- Mermin, N. D. The topological theory of defects in ordered media. *Rev. Mod. Phys.* **51**, 591–648 (1979).
- Giomi, L., Bowick, M. J., Mishra, P., Sknepnek, R. & Cristina Marchetti, M. Defect dynamics in active nematics. *Phil. Trans. A* **372**, 20130365 (2014).
- Giomi, L., Bowick, M. J., Ma, X. & Marchetti, M. C. Defect annihilation and proliferation in active nematics. *Phys. Rev. Lett.* **110**, 209901 (2013).
- de Gennes, P. G. & Prost, J. *The Physics of Liquid Crystals* (Clarendon Press 1993).
- Meyer, R. B. On the existence of even indexed disclinations in nematic liquid crystals. *Phil. Mag.* **27**, 405–424 (1973).
- Jarrell, K. F. & McBride, M. J. The surprisingly diverse ways that prokaryotes move. *Nat. Rev. Microbiol.* **6**, 466–476 (2008).
- Wensink, H. H. et al. Meso-scale turbulence in living fluids. *Proc. Natl Acad. Sci. USA* **109**, 14308–14313 (2012).
- Dunkel, J. et al. Fluid dynamics of bacterial turbulence. *Phys. Rev. Lett.* **110**, 228102 (2013).
- Bertrand, J. J., West, J. T. & Engel, J. N. Genetic analysis of the regulation of type IV pilus function by the Chp chemosensory system of *Pseudomonas aeruginosa*. *J. Bacteriol.* **192**, 994–1010 (2009).
- Oliveira, N. M., Foster, K. R. & Durham, W. M. Single-cell twitching chemotaxis in developing biofilms. *Proc. Natl Acad. Sci. USA* **113**, 6532–6537 (2016).
- Kim, W., Racimo, F., Schluter, J., Levy, S. B. & Foster, K. R. Importance of positioning for microbial evolution. *Proc. Natl Acad. Sci. USA* **111**, E1639–E1647 (2014).
- DellArciprete, D. et al. A growing bacterial colony in two dimensions as an active nematic. *Nat. Commun.* **9**, 4190 (2018).
- Doostmohammadi, A., Thampi, S. P. & Yeomans, J. M. Defect-mediated morphologies in growing cell colonies. *Phys. Rev. Lett.* **117**, 048102 (2016).
- Beroz, F. et al. Verticalization of bacterial biofilms. *Nat. Phys.* **14**, 954–960 (2018).
- Drescher, K. et al. Architectural transitions in *Vibrio cholerae* biofilms at single-cell resolution. *Proc. Natl Acad. Sci. USA* **113**, E2066–E2072 (2016).
- Oldewurtel, E. R., Kouzel, N., Dewenter, L., Henseler, K. & Maier, B. Differential interaction forces govern bacterial sorting in early biofilms. *eLife* **4**, e10811 (2015).
- Anyan, M. E. et al. Type IV pili interactions promote intercellular association and moderate swarming of *Pseudomonas aeruginosa*. *Proc. Natl Acad. Sci. USA* **111**, 18013–18018 (2014).
- Takatori, S. C. & Mandadapu, K. K. Motility-induced buckling and glassy dynamics regulate three-dimensional transitions of bacterial monolayers. Preprint at <https://arxiv.org/abs/2003.05618> (2020).
- Copenhagen, K., Alert, R., Wingreen, N. S. & Shaevitz, J. W. Topological defects induce layer formation in *Myxococcus xanthus* colonies. Preprint at <https://arxiv.org/abs/2001.03804> (2020).
- Grant, M. A. A., Waclaw, B., Allen, R. J. & Cicuta, P. The role of mechanical forces in the planar-to-bulk transition in growing *Escherichia coli* microcolonies. *J. R. Soc. Interface* **11**, 20140400 (2014).
- Yaman, Y. I., Demir, E., Vetter, R. & Kocabas, A. Emergence of active nematics in chaining bacterial biofilms. *Nat. Commun.* **10**, 2285 (2019).
- Pirt, S. J. A kinetic study of the mode of growth of surface colonies of bacteria and fungi. *Microbiology* **47**, 181–197 (1967).

Publisher's note Springer Nature remains neutral with regard to jurisdictional claims in published maps and institutional affiliations.

© The Author(s), under exclusive licence to Springer Nature Limited 2020

Methods

Bacterial strains and fluorescent labelling. The clean deletion mutants and the corresponding WT strains^{17,31} used in this study were labelled with either cyan fluorescent protein (CFP) or yellow fluorescent protein (YFP) using a Gm^r mini-Tn7 vector³², using a three-strain mating protocol. Briefly, *P. aeruginosa* colonies were grown overnight at 42 °C on an LB (Lennox, 20 g l⁻¹, Fisher Scientific) plate containing 1.5% (w/v) agar (Difco brand, BD). These were then mixed with both the mini-Tn7 donor *Escherichia coli* strain and an SM10 λpir *E. coli* helper strain on the surface of a fresh LB agar plate. The resulting mixed three-strain plate was incubated overnight at 30 °C. Cells were then resuspended in liquid LB and transformants selected on LB agar plates containing both gentamicin (30 mg l⁻¹) and kanamycin (25 mg l⁻¹). The resulting CFP- and YFP-labelled strains were then directly competed with unlabelled strains to confirm that the impact of the labelling process on growth rate and motility was negligible (Extended Data Fig. 8a).

Bacterial cell culture. We streaked -80 °C freezer stocks onto LB agar plates and incubated them overnight at 37 °C. Single colonies were picked and grown overnight in liquid LB at 37 °C under continuous shaking. The following day, overnight cultures were diluted 30-fold in fresh LB broth and returned to the 37 °C shaking incubator for 2 h to obtain cells in exponential phase. Immediately before being used in colony experiments, the optical density at 600 nm (OD₆₀₀) was adjusted to 0.05 (approximately 12,500 cells per μl) using fresh LB. For co-culture experiments, the optical densities of cultures of each individual strain were adjusted to OD₆₀₀ = 0.05. These were then mixed in a single tube to ensure both strains were present in equal proportion. All colony-based assays were conducted at room temperature using LB agar composed of 5 g l⁻¹ NaCl (Fisher Scientific), 5 g l⁻¹ yeast extract (Bacto brand, BD) and 10 g l⁻¹ tryptone (Bacto brand, BD), solidified with either 0.8% (w/v, subsurface assays unless otherwise specified) or 1.5% (w/v, surficial assays) agar.

Microscopic imaging. We used three microscopes in this study: two higher-magnification inverted microscopes (denoted as ‘Zeiss inverted’ and ‘Nikon inverted’ within this text and Supplementary Methods) and a lower-magnification stereo zoom microscope (‘Zeiss zoom’). Specifications of these instruments are provided in Supplementary Table 1.

Surficial colony competition assays. Surficial colonies were inoculated with a liquid culture containing an equal fraction of two different strains, as described above. We spotted 10 μl exponential phase culture onto a freshly poured 1.5% (w/v) LB agar plate and sealed the plate lids with Parafilm (Bemis) to prevent evaporation. The surficial colonies in which we evaluated the distribution and orientation of cells using scanning laser confocal microscopy (Extended Data Fig. 2b,c) were incubated at room temperature for 16 h, ensuring that the colony was still sufficiently thin that its entire thickness could be imaged. In contrast, the surficial colonies used to quantify the relative fitness of WT/ $\Delta pilH$ cells and their macroscopic distribution (Fig. 2a,b) were incubated at room temperature for 48 h.

We calculated the average number of cell divisions of each strain over the 48 h of competition using the expression:

$$\text{Number of cell divisions} = \log_2 \left(\frac{\text{Number of cells of strain in colony after 48 h}}{\text{Number of cells of strain inoculated onto surface}} \right). \quad (1)$$

We measured the number of cells of each strain used to inoculate the surface by diluting the mixed liquid cultures used for inoculation and then spreading them onto LB plates. The resulting colonies were counted manually after incubation overnight using the Zeiss zoom microscope, which allowed us to distinguish YFP- and CFP-expressing colony forming units (CFUs).

A similar technique was used to estimate the number of cells of each strain in each colony after 48 h of incubation. Whole surficial colonies were scraped, resuspended in fresh media and vortexed. The resulting suspensions were then diluted, spread onto LB plates and incubated overnight. We again used the Zeiss zoom microscope to manually enumerate the number of CFUs expressing either YFP or CFP.

We imaged the colonies after 48 h of competition to visualize the distribution of the two different strains. *P. aeruginosa* natively produces secretions called siderophores that have excitation and emission spectra similar to CFP^{33,34}. While individual CFP- and YFP-labelled cells can easily be distinguished in the monolayer of subsurface colonies (Fig. 2g), surficial colonies are thicker, incubated for longer and must be imaged with lower-resolution objectives (owing to the lack of a coverslip). These three factors made it difficult to distinguish CFP-labelled cells from siderophore secretions in surficial colonies. To circumvent this problem, we imaged surficial colonies using a combination of brightfield and YFP fluorescence, such that regions with a larger fraction of CFP cells appeared darker grey in the merged brightfield/YFP images (Fig. 2a).

Subsurface assays. We prepared subsurface colonies using a protocol similar to one previously described³⁵. Briefly, a pad of LB agar was cut from a freshly poured plate and transferred to a glass slide. We used an agar concentration of 0.8% (w/v), unless otherwise specified (Extended Data Fig. 10). The pad was spotted with a 1 μl drop of bacterial culture adjusted to an optical density of OD₆₀₀ = 0.05, which was

then allowed to dry until fully evaporated. The pad was then carefully inverted and placed into a coverslip-bottomed Petri dish (175 μm coverslip thickness, MatTek), sandwiching the cells between agar and the glass coverslip. By fully enclosing the agar pad, these dishes prevented evaporation and agar shrinkage over the course of the experiment. We found it was essential to use freshly poured agar to ensure consistency between experiments. We note that the bacterial culture was spotted onto the side of the agar that was facing up when it was initially poured (that is, the side that was exposed to air rather than the side against the plastic Petri dish).

Experiments with cells that lack pili ($\Delta pilB$ ³⁷; Fig. 1f,g) and flagella ($\Delta flgK$ ³⁶; Extended Data Fig. 1a,b) indicate that the cells in our assays move solely via pili-based motility. While cells can swim in agar at low concentrations³⁷, we found that the lowest concentration of agar used in our experiments (0.8%) suppressed flagella-based motility. $\Delta flgK$ cells, which lack flagella, form subsurface colonies under 0.8% agar that actually expand at a faster rate than WT cells, verifying that the colony expansion observed in our assay is not driven by flagellar motility (Extended Data Fig. 1a,b). This finding is consistent with previous work that shows mutants lacking flagella exhibit more rapid twitching motility than WT cells¹⁸, probably because flagella tend to adhere to surfaces.

A detailed description of each type of assay performed in the subsurface environment is provided in Supplementary Methods.

Imaging rosette formation. Quantifying the movement of both defects and individual cells during the process of rosette formation (Fig. 4d–f, Extended Data Fig. 7 and Supplementary Video 9) was exceptionally challenging, as it required imaging the monolayer at high spatial resolution ($\times 63$ magnification, two frames per minute) at precisely the time and place that rosettes begin to form. It was difficult to estimate a priori where rosette formation would occur and thus where to place the Zeiss inverted microscope’s relatively small field of view to capture these events.

To maximize our chances of success, we inoculated multiple $\Delta pilH$ -YFP/WT-CFP subsurface colonies with 10 μl of culture at a range of different optical densities (OD₆₀₀) in a six-well coverslip-bottomed plate (175 μm coverslip thickness, MatTek). We then imaged the monolayer of each colony in turn, starting from the colony initiated with the culture at the highest optical density. As rosettes form earlier in colonies inoculated at higher densities, this provided multiple opportunities to image the monolayer precisely at the moment that rosette formation begins.

Initially, we attempted to take time-lapse images of rosette formation using fluorescent confocal microscopy so we could use their YFP and CFP labels to continuously follow how the two strains were distributed. However, this bleached the cells and adversely affected their movement. Instead, we imaged the dynamics of rosette formation using brightfield microscopy for a period of 1 h (Supplementary Video 9). After rosettes had formed, we then immediately switched over to fluorescent confocal imaging, which allowed us to quantify the distribution and orientation of the two different strains within the same rosette (Fig. 4f). Both brightfield and confocal microscopy were performed on the Zeiss inverted microscope.

Liquid culture competition assay. To compare the growth rate of mutants (Extended Data Fig. 8b), we grew the different strains in liquid culture and estimated their fitness relative to a WT reference strain by counting CFUs. We mixed a CFP-labelled WT reference strain with YFP-labelled $\Delta pilH$, $\Delta pilB$ and WT test strains in a 1:1 ratio. Liquid cultures were started at OD₆₀₀ = 0.02 and placed in a shaking incubator at 23 °C, the same temperature used in the subsurface colony experiments. We counted the number of YFP- and CFP-expressing CFUs after $t = 0, 210$ and 420 min of competition to calculate the relative fitness, w , of the YFP test strain compared with that of the CFP control:

$$w = \frac{\ln(C_Y(t)/C_Y(0))}{\ln(C_C(t)/C_C(0))}, \quad (2)$$

where $C_Y(0)$ and $C_C(0)$ are respectively the numbers of YFP and CFP cells measured at the beginning of the competition, and $C_Y(t)$ and $C_C(t)$ are the numbers of YFP and CFP cells at time t .

Measurement of cell length in liquid cultures. To measure the lengths of cells in liquid culture (Extended Data Fig. 6a), we combined exponentially growing cultures of $\Delta pilH$ -YFP and WT-CFP at a 1:1 ratio. These were fixed with 3% paraformaldehyde and then diluted in phosphate buffered saline (Fisher Scientific) in 96-well plates with optical bottoms (Nunc brand, Thermo Scientific). We then centrifuged plates to ensure that cells were oriented flat against the optical bottoms of the wells and imaged them in brightfield, YFP and CFP channels at $\times 63$ magnification using the Zeiss inverted microscope. Cell lengths were then measured using our FAST software (see below).

Quantification of subsurface colonies. Our automated measurements of colony edge positions (Figs. 1f,g and 2d and Extended Data Figs. 1a,b and 9b), cell-packing fractions (Fig. 2e and Extended Data Fig. 10a) and strain composition (Fig. 2f and Extended Data Figs. 9c and 10b) were performed using custom MATLAB (Mathworks) scripts, which have been made publicly available as the colEDGE package (see Code availability statement below). For a detailed

description of the techniques used in this package, see the Supplementary Methods and Supplementary Fig. 1.

Single-cell tracking. We attempted to use existing software packages to track movement of individual cells within the monolayer of our subsurface colony experiments. As a single monolayer image can contain more than 10,000 cells, we found existing software packages (most of which are designed for tracking sparse objects at low density) were prohibitively slow and/or were incapable of correctly segmenting individual cells when they are tightly packed together. Obtaining an accurate segmentation under these densely packed conditions is particularly challenging because the boundaries that separate neighbouring cells tend to be both thin and very faint.

To overcome these problems, we developed a new MATLAB-based tracking platform named FAST³⁸ (Feature-Assisted Segmenter/Tracker). In brief, FAST uses a standard tracking by detection framework³⁹. First, individual cells are isolated from their neighbours using a sequence of segmentation routines. Next, we measure the ‘features’ of each cell within each frame (including cell position, orientation, morphology and fluorescence intensity). Finally, we use these features to follow individual cells between frames using an algorithm that automatically trains itself using unsupervised machine learning to optimize tracking based on the available feature information.

In the segmentation stage, we use brightfield images to identify individual cells in the monolayer. Our software uses a combination of automated ridge detection⁴⁰, topographical watershed⁴¹ and intensity thresholding to generate black and white binary images of cells that are not connected to one another. Using this binary image as a mask, we then extract each cell’s features from the original brightfield image.

Tracking is achieved via a two-stage algorithm. In the first stage, a low-fidelity nearest-neighbour tracking algorithm is used to generate a set of putative links between objects in consecutive frames. The subset of links with the smallest corresponding frame–frame object displacements is then classified as ‘correct’, typically forming around half of the total putative links. This subset forms the training dataset. Statistical parameters are then extracted from this training dataset, allowing us to quantify how robust each feature is as a marker of object identity and thus quantify its utility in linking objects between sequential frames. In the second stage of the tracking algorithm, these measurements are used to dynamically adjust the weighting of each feature such that unreliable features have a reduced weighting compared with more reliable features. Tracking is then repeated, using these reweighted features as inputs. This approach allowed us to obtain extremely large tracking datasets, for example, yielding a total of 161,769 cell trajectories for a single video of the WT monolayer.

We note that while FAST has primarily been developed for tracking of single cells in dense monolayers, its capabilities can also be leveraged to analyse other datasets. For example, FAST can also be used to track topological defects through time and space (see following section).

Detection and analysis of topological defects. Comets and trefoils occur at singularities in cell orientation. Our automated approach for locating these singularities is similar to that described in ref. ⁴²: in the first stage, we used the OrientationJ plugin for Fiji⁴³ to measure the local orientation of cells using the tensor method⁴⁴. Experimental images of the monolayer were loaded into Fiji and directly analysed using OrientationJ. For consistency, we also used the same defect analysis pipeline to analyse the output of our 2D SPR model: a time series of images was created by drawing rods as grey ellipses on a white background. These images were then processed using OrientationJ in the same way as for our experimental images. To facilitate direct comparison between our experiments and simulations, we set the size of the structure tensor window, which defines the spatial scale over which the orientation field is calculated, to a length equivalent to two cell/rod widths. This process yields the orientation of cells, $\theta = [-\pi/2, \pi/2]$ at each pixel in the input image (Fig. 3b).

The position, orientation and topological charge of defects was quantified using our custom package known as Defector (see Code Availability statement below and Supplementary Methods). We next used FAST to track the movement of defects using these three quantities as ‘features’ (see above). To reduce noise, defects that were present for fewer than five timepoints were excluded from our analyses. This analysis yielded a total set of 1,344 trefoil trajectories and 1,382 comet trajectories. The RMSD of tracked trefoils and comets was calculated using:

$$R(\tau) = \sqrt{\langle (x(t+\tau) - x(t))^2 + (y(t+\tau) - y(t))^2 \rangle}. \quad (3)$$

where τ is the lag time, (x, y) is the position of the defect, and $\langle \cdot \rangle$ denotes an ensemble average across all times t and across all defect trajectories.

True to its name, pili-based ‘twitching’ motility is jerky and highly unsteady, owing to the stochastic retraction and detachment of individual pili^{6,45}. Obtaining a reliable measure of cell movement around defects thus required averaging of data across a large number of defects and cell trajectories so that the stochastic component of each cell’s movement was averaged out.

To accomplish this, we first tracked the movement of defects and cells independently from one another. Next, we transformed the coordinate system

of each cell trajectory so that its origin and orientation were measured relative to the centre and orientation of a nearby defect. This allowed us to combine cell trajectories collected from around a large number of different comet and trefoil defects. After the cell trajectories were aligned with one another in the same reference frame, we averaged the cell velocities in a 2D array of bins. The size of each bin was $3.2 \mu\text{m} \times 3.2 \mu\text{m}$. All velocity measurements were made with respect to the laboratory reference frame, not the reference frame of the defect.

We calculated the flow field around defects in the SPR model in the same way as for the experiments, though rod trajectories were obtained directly from the model output, rather than from our FAST tracking software. To facilitate direct comparison between the SPR model and experiments, we normalized the flow-field velocities around defects by dividing them by the average speed of all cells within the simulation or field of view, respectively.

Quantification of collective cell motility during rosette development. While our FAST software can track horizontally oriented cells in the monolayer of colonies, once cells had reoriented perpendicular to the surface it was exceedingly difficult to distinguish individual cells. Instead of single-cell tracking, we therefore characterized the collective movement of cells during rosette formation using a technique known as particle image velocimetry (PIV), which operates on a coarse-grained level and does not require the segmentation of individual cells.

PIV analysis was conducted on a 1-h-long time series of $\times 63$ magnification images recorded during the process of rosette formation. Images were pre-processed using contrast normalization and manually stabilized to remove thermally induced drift in the x - y plane. The resulting images were analysed using PIVlab, an open-source MATLAB-based software⁴⁶. We filtered our results using PIVlab’s built-in tools to remove spurious data points. Specifically, velocity vectors that exceeded $0.6 \mu\text{m min}^{-1}$ were removed and replaced with velocities interpolated from neighbouring points, which helped to reduce noise. The resulting measurements of instantaneous velocity were then averaged over the entire 1 h period (Fig. 4e and Extended Data Fig. 7a).

SPR simulations. Our individual-based SPR simulations are based on a previously described model^{15,47}. In brief, cells are modelled as rigid rods, which repel each other through an interaction potential, U . In addition, rods are self-propelled by a force, F , acting along their axis. In the 2D SPR model used to generate Fig. 3d, the equations of motion that determine how the position \mathbf{r}_α and orientation θ_α of rod α changes over time are given by:

$$f_T \frac{\partial \mathbf{r}_\alpha}{\partial t} = -\frac{\partial U_\alpha}{\partial \mathbf{r}_\alpha} + F \hat{\mathbf{u}}_\alpha, \quad (4a)$$

$$f_\theta \frac{\partial \theta_\alpha}{\partial t} = -\frac{\partial U_\alpha}{\partial \theta_\alpha}, \quad (4b)$$

where f_T is the translational friction tensor, f_θ is the rotational friction constant and $\hat{\mathbf{u}}_\alpha$ is the orientational unit vector ($\hat{\mathbf{u}}_\alpha = (\cos(\theta_\alpha), \sin(\theta_\alpha))$).

During rosette formation, cells can reorient out of the plane. To model this process, we give the rods in our simulations an additional degree of freedom, by allowing them to change their polar angle ϕ with respect to the 2D plane. The equation of motion for ϕ is similar to that for the azimuthal angle θ , but must additionally take into account the elastic restoring force imposed by the overlying agar and extracellular polymeric secretions that act to keep cells oriented flat against the surface^{48,49}. Taking these into account, we arrive at the third equation of motion:

$$f_\phi \frac{\partial \phi}{\partial t} = -\frac{\partial U_\alpha}{\partial \phi} + \frac{k l^2}{2} \cos \phi_\alpha \sin \phi_\alpha, \quad (5)$$

where k is the stiffness of the overlying substrate and l is the length of the rod. This additional governing equation is used in the simulations presented in Fig. 4a–c and Extended Data Figs. 5 and 6b–e. Further details about these simulations and a more detailed derivation of equation (5) can both be found in Supplementary Methods.

Reporting Summary. Further information on research design is available in the Nature Research Reporting Summary linked to this article.

Data availability

Source data for Figs. 1–4 and Extended Data Figs. 1, 3–6 and 8–10 are provided with the paper. In addition, the data that support the findings of this study can be accessed at <https://doi.org/10.15131/shef.data.12735251.v1>.

Code availability

The FAST cell-tracking package can be accessed at <https://doi.org/10.5281/zenodo.3630641>, with extensive documentation on its use and functionality available at https://mackdurham.group.shef.ac.uk/FAST_DokuWiki/dokuwiki. The Defector defect detection package is available at <https://doi.org/10.5281/zenodo.3974873>, while the colEDGE colony composition package can be accessed at <https://doi.org/10.5281/zenodo.3974875>. The MATLAB-based implementation of the 3D SPR model can be accessed at <https://doi.org/10.5281/zenodo.4139459>.

References

31. O'Toole, G. A. & Kolter, R. Flagellar and twitching motility are necessary for *Pseudomonas aeruginosa* biofilm development. *Mol. Microbiol.* **30**, 295–304 (1998).
32. Choi, K.-H. & Schweizer, H. P. mini-Tn7 insertion in bacteria with single *attTn7* sites: example *Pseudomonas aeruginosa*. *Nat. Protoc.* **1**, 153–161 (2006).
33. Cox, C. D. & Graham, R. Isolation of an iron-binding compound from *Pseudomonas aeruginosa*. *J. Bacteriol.* **137**, 357–364 (1979).
34. Elliott, R. P. Some properties of pyoverdine, the water-soluble fluorescent pigment of the pseudomonads. *Appl. Microbiol.* **6**, 241–246 (1958).
35. Darzins, A. The *pilG* gene product, required for *Pseudomonas aeruginosa* pilus production and twitching motility, is homologous to the enteric, single-domain response regulator CheY. *J. Bacteriol.* **175**, 5934–5944 (1993).
36. O'Toole, G. A. & Kolter, R. Initiation of biofilm formation in *Pseudomonas fluorescens* WCS365 proceeds via multiple, convergent signalling pathways: a genetic analysis. *Mol. Microbiol.* **28**, 449–461 (1998).
37. Wolfe, A. J. & Berg, H. C. Migration of bacteria in semisolid agar. *Proc. Natl Acad. Sci. USA* **86**, 6973–6977 (1989).
38. Meacock, O. J. & Durham, W. M. Pseudomoaner/FAST v0.9.1. *Zenodo* <https://doi.org/10.5281/ZENODO.3630642> (2020).
39. Li, K. et al. Cell population tracking and lineage construction with spatiotemporal context. *Med. Image Anal.* **12**, 546–566 (2008).
40. Lindeberg, T. Edge detection and ridge detection with automatic scale selection. *Int. J. Comput. Vis.* **30**, 117–156 (1998).
41. Meyer, F. Topographic distance and watershed lines. *Signal Process.* **38**, 113–125 (1994).
42. Kawaguchi, K., Kageyama, R. & Sano, M. Topological defects control collective dynamics in neural progenitor cell cultures. *Nature* **545**, 327–331 (2017).
43. Schindelin, J. et al. Fiji: an open-source platform for biological-image analysis. *Nat. Methods* **9**, 676–682 (2012).
44. Püspöki, Z., Storath, M., Sage, D. & Unser, M. in *Focus on Bio-Image Informatics* (eds. Vos, W. H. et al.) 69–93 (Springer, 2016).
45. Jin, F., Conrad, J. C., Gibiansky, M. L. & Wong, G. C. L. Bacteria use type-IV pili to slingshot on surfaces. *Proc. Natl Acad. Sci. USA* **108**, 12617–12622 (2011).
46. Thielicke, W. & Stamhuis, E. J. PIVlab—towards user-friendly, affordable and accurate digital particle image velocimetry in MATLAB. *J. Open Res. Softw.* **2**, e30 (2014).
47. Wensink, H. H. & Löwen, H. Emergent states in dense systems of active rods: from swarming to turbulence. *J. Phys. Condens. Matter* **24**, 464130 (2012).
48. Zhao, K. et al. Psl trails guide exploration and microcolony formation in *Pseudomonas aeruginosa* biofilms. *Nature* **497**, 388–391 (2013).
49. Nayar, V. T., Weiland, J. D., Nelson, C. S. & Hodge, A. M. Elastic and viscoelastic characterization of agar. *J. Mech. Behav. Biomed. Mater.* **7**, 60–68 (2012).
50. Shi, X. & Ma, Y. Topological structure dynamics revealing collective evolution in active nematics. *Nat. Commun.* **4**, 3013 (2013).

Acknowledgements

We thank S. Booth, N. Clarke, C. Durham, A. Fenton, E. Granato, J. Guasto, J. Hobbs, T. Meiller-Legrand, W. Smith, A. Morozov and J. Wheeler for providing comments on a previous version of this manuscript, R. Allen and R. Hawkins for helpful discussions, W. Smith for assistance with the SPR model, J. Engel for sharing bacterial strains, and M. Hopkins for assistance with preliminary experiments. O.J.M. was supported by an EPSRC studentship through the Life Sciences Interface Centre for Doctoral Training (EP/F500394/1); A.D. was supported by the Novo Nordisk Foundation (grant number NNF18SA0035142), Villum Fonden (grant number 29476), Danish Council for Independent Research, Natural Sciences (DFF-117155-1001), and the European Unions Horizon 2020 research and innovation programme under the Marie Skłodowska-Curie grant agreement number 847523 (INTERACTIONS); K.R.F. was supported by European Research Council grant 787932 and Wellcome Trust Investigator award 209397/Z/17/Z; and W.M.D. was supported by a startup grant from the University of Sheffield's Imagine: Imaging Life initiative, an EPSRC Pump Priming Award (EP/M027430/1) and a BBSRC New Investigator Grant (BB/R018383/1).

Author contributions

O.J.M. performed experiments, implemented the SPR model, analysed data and prepared figures. A.D. and J.M.Y. proposed the mechanism of rosette formation. O.J.M., A.D., K.R.F., J.M.Y. and W.M.D. all contributed to the design of experiments and models, as well as to the interpretation of results. O.J.M., K.R.F. and W.M.D. wrote the paper with input from A.D. and J.M.Y. This collaborative effort was led by W.M.D.

Competing interests

The authors declare no competing interests.

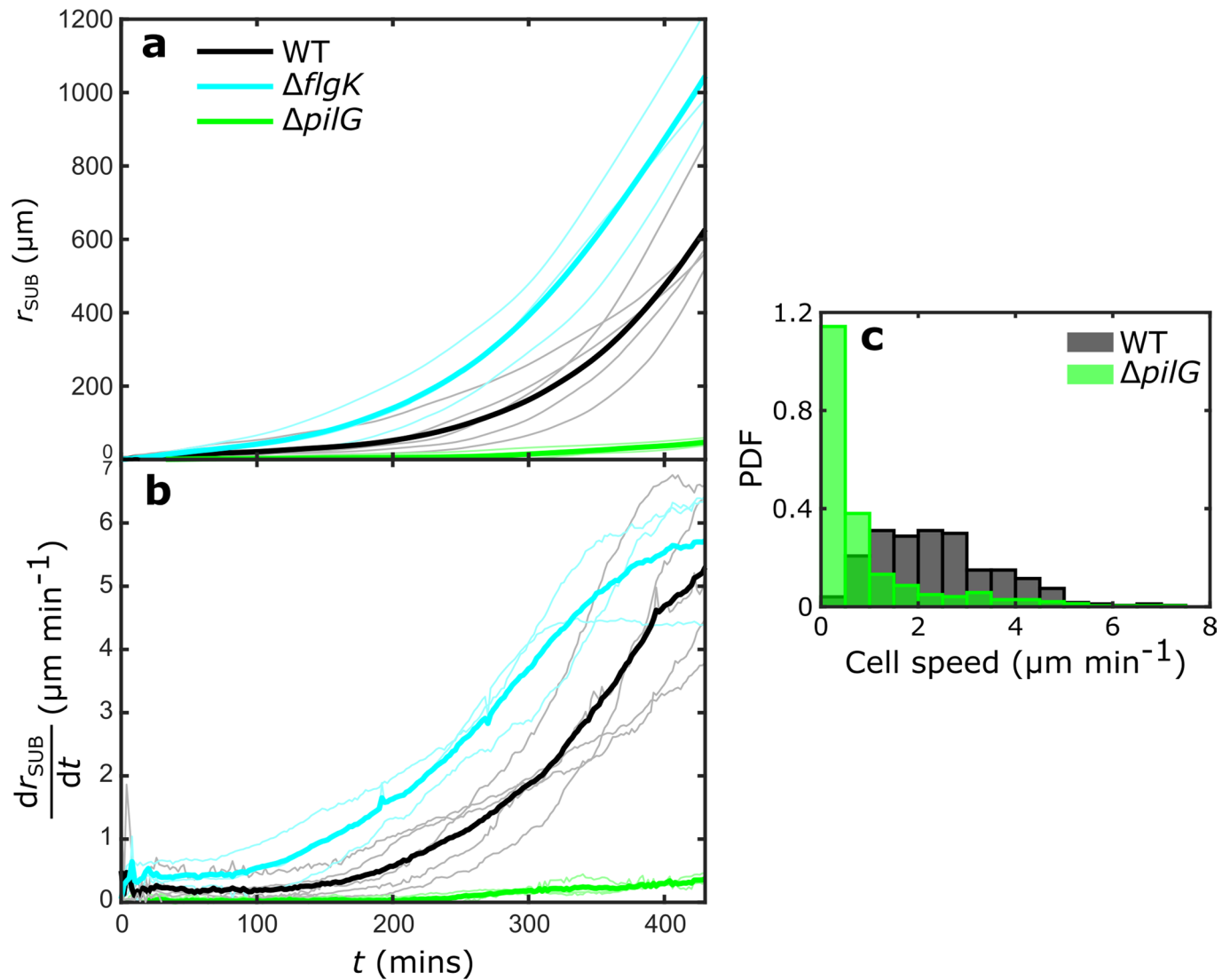
Additional information

Extended data is available for this paper at <https://doi.org/10.1038/s41567-020-01070-6>.

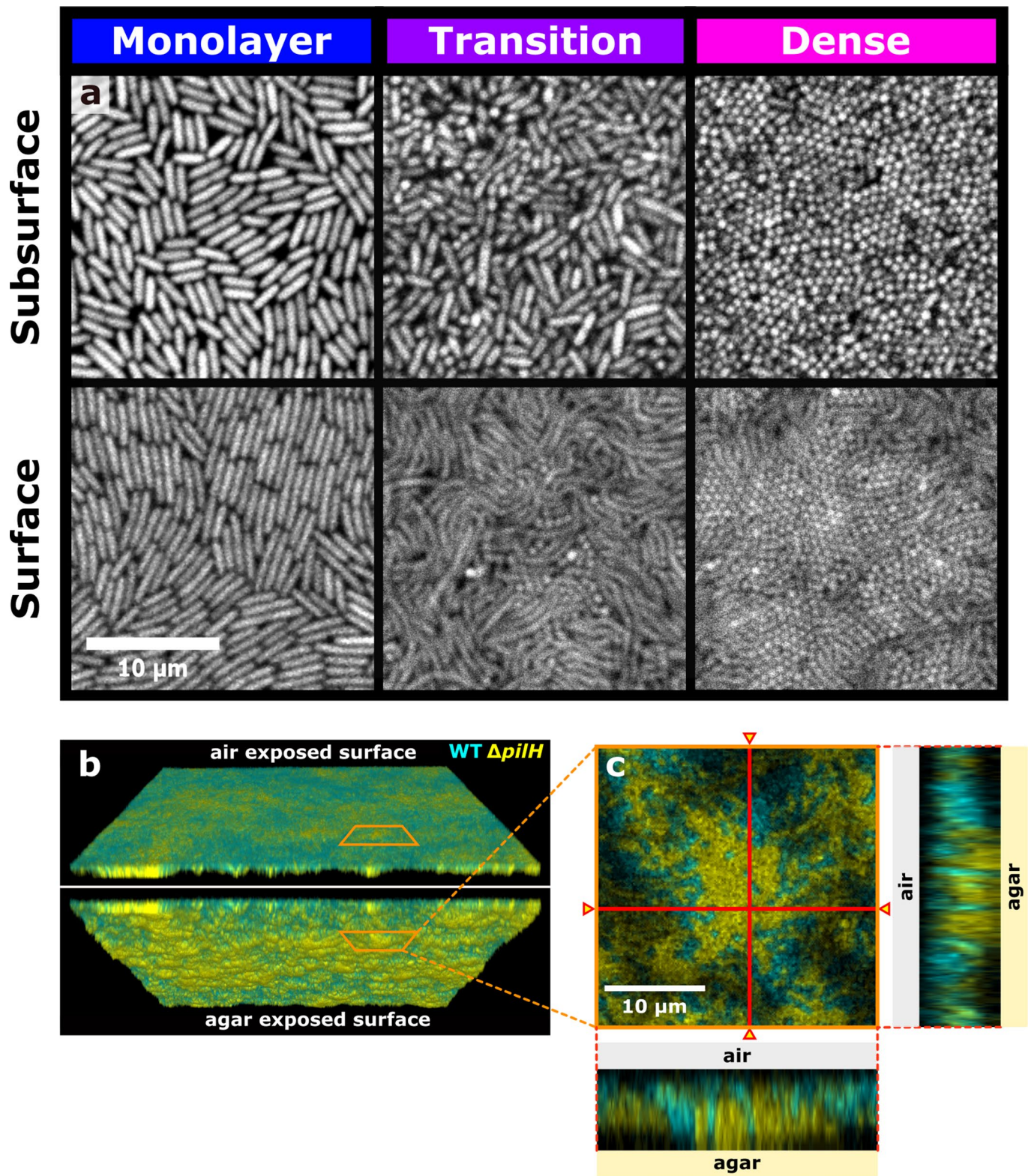
Supplementary information is available for this paper at <https://doi.org/10.1038/s41567-020-01070-6>.

Correspondence and requests for materials should be addressed to K.R.F., J.M.Y. or W.M.D.

Reprints and permissions information is available at www.nature.com/reprints.

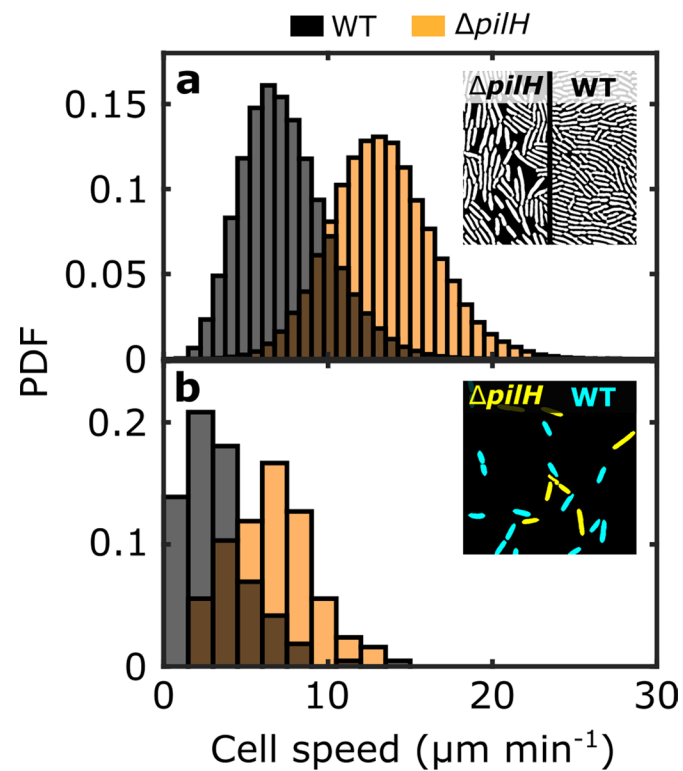


Extended Data Fig. 1 | In the subsurface environment, colonies composed of cells lacking flagella expand faster than those of WT cells, while pili-based chemotaxis mutants display little, if any, motility. a, b, Measurements of the colony radius, r_{SUB} , and colony expansion rate, $\frac{dr_{SUB}}{dt}$, for the wild-type (WT, black, $n = 5$), a non-flagellated mutant ($\Delta flgK$, cyan, $n = 3$) and a mutant previously shown to be incapable of performing pilus-based chemotaxis in microfluidic devices¹⁸ ($\Delta pilG$, green, $n = 3$). Thick lines indicate the mean of n different colonies. Comparison of $\Delta flgK$ and WT data indicate that flagella actually hinder colony expansion. We speculate this is because flagella actively stick to surfaces¹⁸, increasing the cells' resistance to movement. **c**, Single-cell speed distributions of WT ($n = 347$) and $\Delta pilG$ cells ($n = 483$) when mixed together at low cell density. The speed of solitary $\Delta pilG$ cells was significantly smaller than that of solitary WT cells ($p < 10^{-68}$, Mann-Whitney U test), demonstrating that the slow expansion of $\Delta pilG$ colonies is caused by a more general defect in their motility, rather than a lack of chemotaxis. $\Delta pilG$ cells express few pili¹⁷, which likely impedes their ability to move in high friction environments like those found in agar-based subsurface assays.

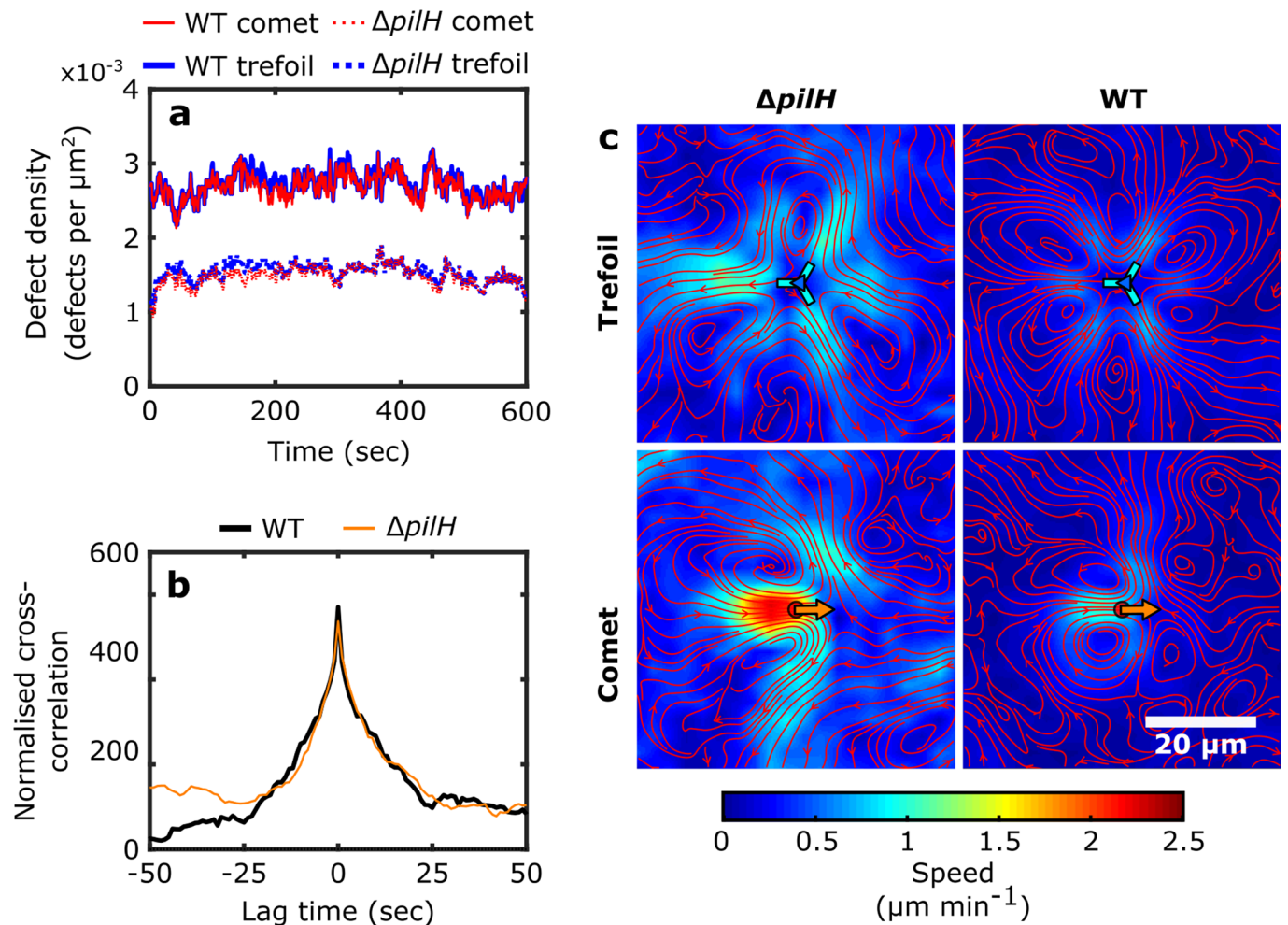


Extended Data Fig. 2 | See next page for caption.

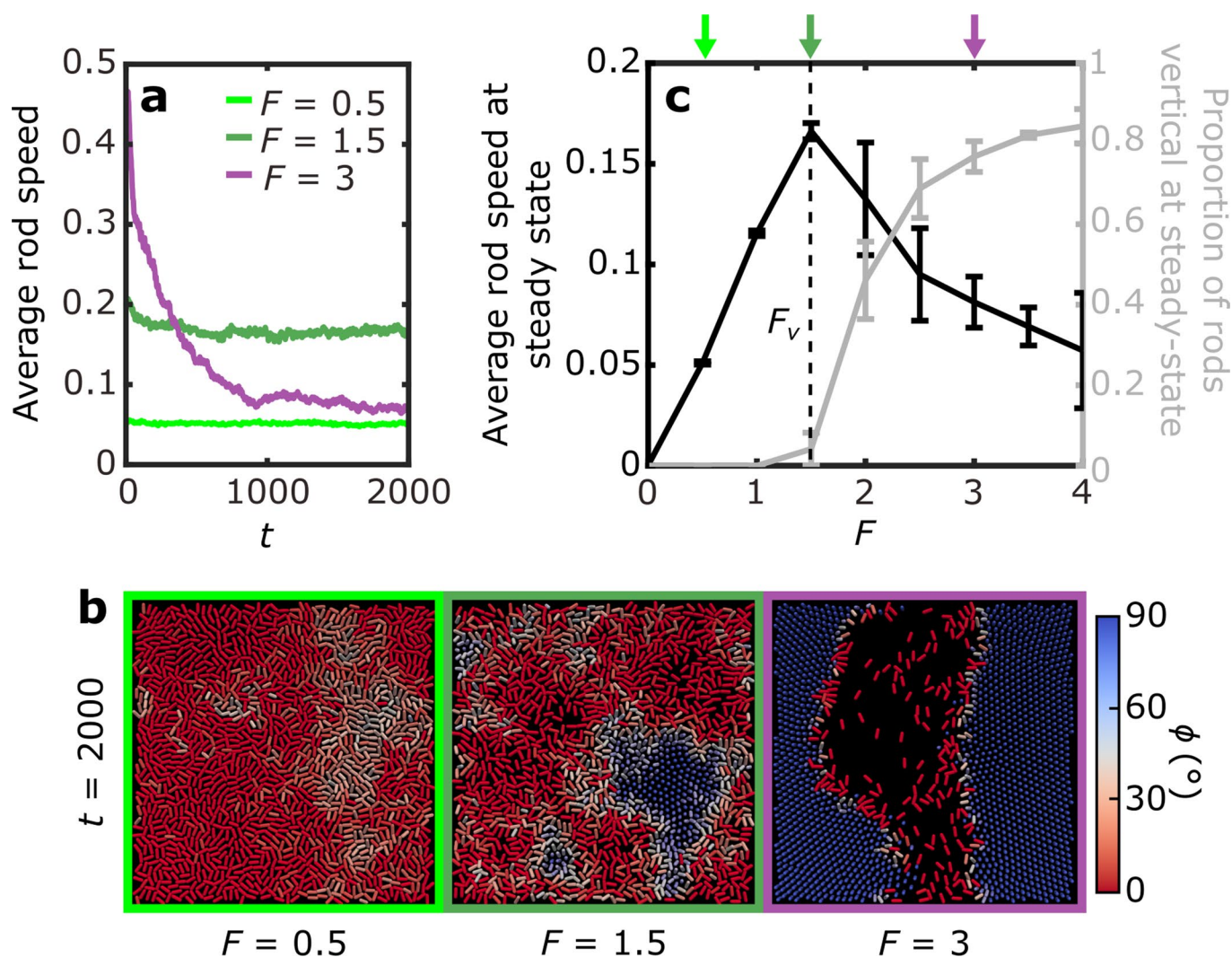
Extended Data Fig. 2 | Cells have similar orientations in both subsurface and surficial colonies. **a**, Surficial and subsurface colonies of YFP labelled WT cells were grown for 24 h at room temperature and then imaged using confocal microscopy (Methods). Both subsurficial (upper row) and surficial (lower row) colonies have a 'monolayer' of cells lying flat against the surface at their periphery, a 'dense' region where most cells are vertically standing up on end at their center, and a 'transition' region where some cells are standing up between the colony edge and center (Fig. 1b-d). We note that subsurface colony images shown here are the same as those presented in Fig. 1d, but are reproduced here to facilitate direct comparison. **b**, Volumetric projections of a confocal image of a surficial colony inoculated with equal fractions of WT-CFP and $\Delta pilH$ -YFP cells. In the upper projection, the three-dimensional image is tilted to show the upper air-exposed surface of the colony, while in the lower projection the image is tilted in the opposite direction to show the side of the colony facing the agar. As the thickness of surficial colonies increases over time, we imaged the colony 16 h after inoculation while it was still sufficiently thin to visualise its entire depth using confocal microscopy. Each edge of the imaged region is 170 μm long. A zoomed-in view of the region within the orange boxes (**c**) shows that nearly all of the vertically oriented cells protruding into the agar below are $\Delta pilH$ -YFP cells, while WT-CFP cells tend to remain horizontal along the air-exposed surface. Orthogonal views show cross sections through the colony at the locations marked by the red lines. These images demonstrate that $\Delta pilH$ tends to form structures in surficial colonies similar to those observed in subsurface colonies (Fig. 4f).



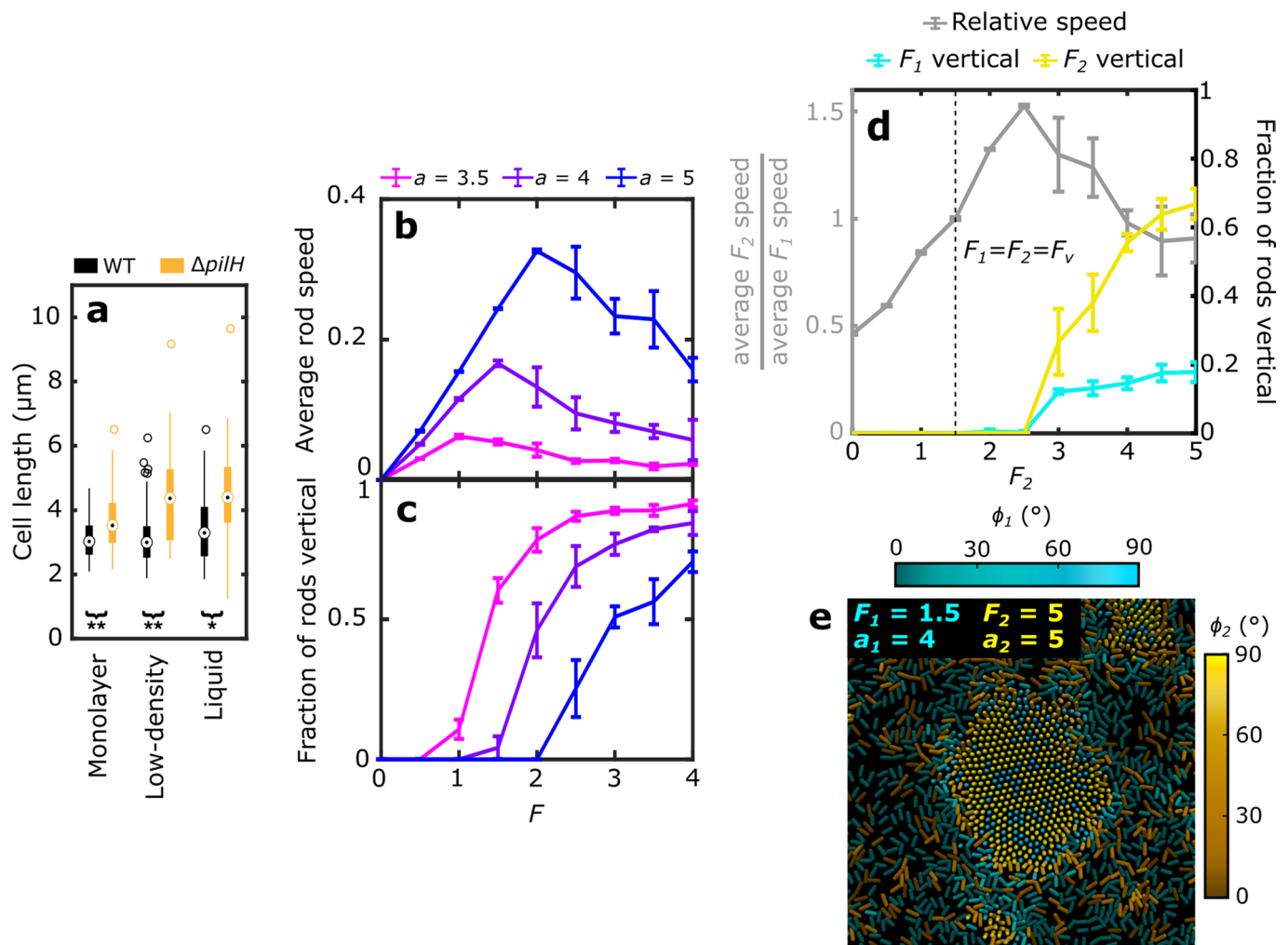
Extended Data Fig. 3 | $\Delta pilH$ cells move faster than WT cells. Cells in the monolayer of $\Delta pilH$ colonies move faster than those in WT colonies (Fig. 1e, reproduced in **a**). However, $\Delta pilH$ monolayers are also observed to have a smaller packing fraction than WT monolayers (**a**, inset). To test if the variation in cell density could confound our analyses, we also performed a separate experiment in which $\Delta pilH$ and WT cells were mixed together at low density. Separate fluorescent markers were used to distinguish strains (**b**, inset). This confirmed that $\Delta pilH$ cells move more quickly than WT cells when the two are at equal density ($p < 10^{-17}$, Mann-Whitney U test). All experiments shown were performed using the subsurface assay.



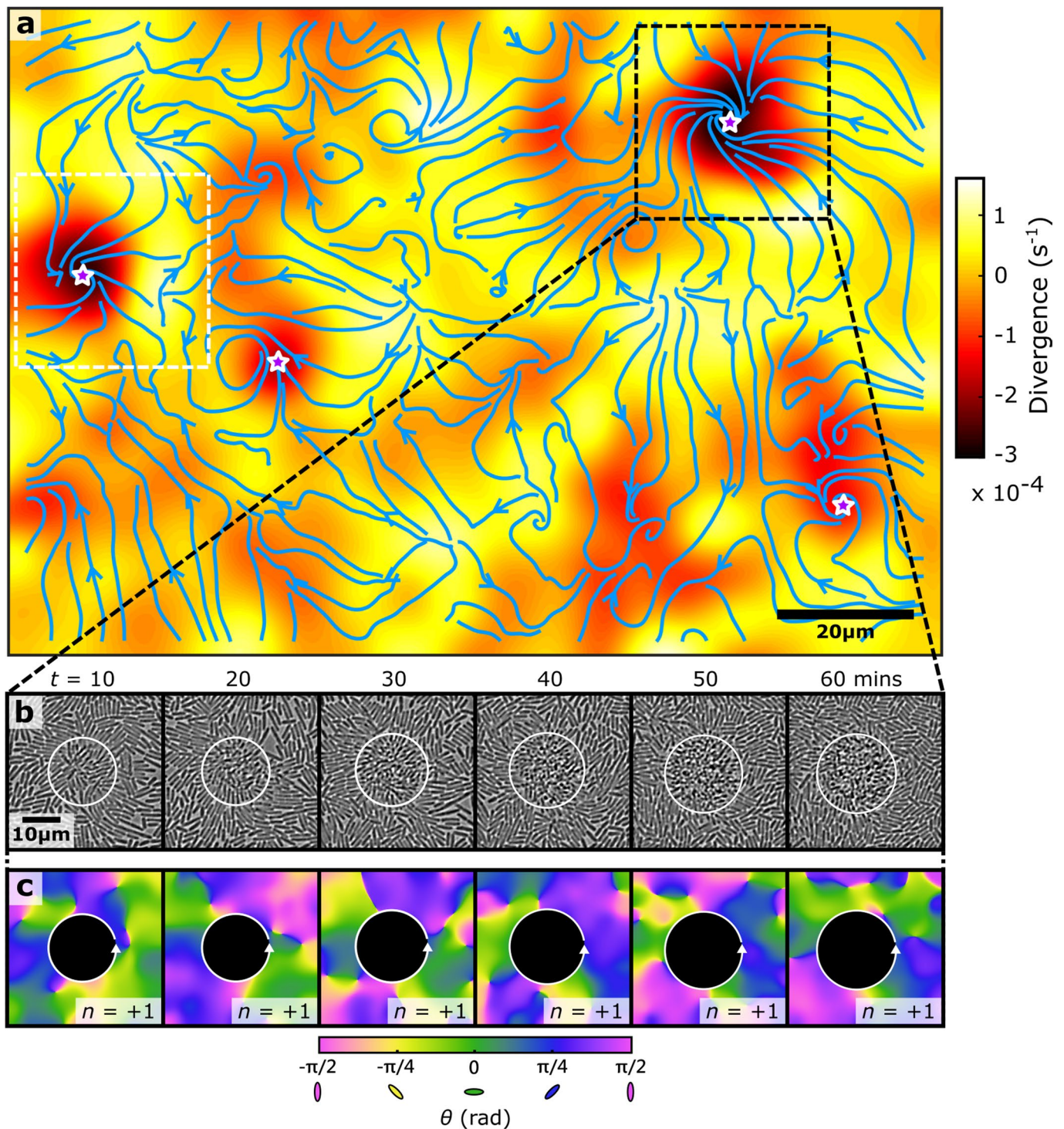
Extended Data Fig. 4 | Automated analysis of defects reveals differences between the collective motility of WT and $\Delta pilH$ monolayers. **a**, We used automated defect detection to count the number of comets/trefoils in monolayers of both genotypes and normalized these by the area of the field of view (Methods). Averaging over time, we found that WT monolayers contain 79% more defects than $\Delta pilH$ monolayers. Fluctuations in the numbers of comets and trefoils closely follow one another, as predicted by the Poincaré-Hopf theorem which requires that the total topological charge of the system must remain fixed⁹. **b**, This relationship was quantified further by calculating the normalized cross-correlation between comet and trefoil density. The maximum cross-correlation occurs at a lag time of zero for both strains, indicating that comet/trefoil pairs are created and annihilated instantaneously. This matches predictions made by previous SPR simulations⁵⁰. **c**, Timeseries of $\Delta pilH$ and WT monolayers were processed to obtain measurements of the average flow of cells around comets and trefoils as for Fig. 3d. While the same characteristic flow structures were observed in both strains, we observed that the magnitude of the flow velocity was larger for the $\Delta pilH$ monolayer. This is consistent with $\Delta pilH$ monolayers having a larger activity than WT monolayers¹⁰.



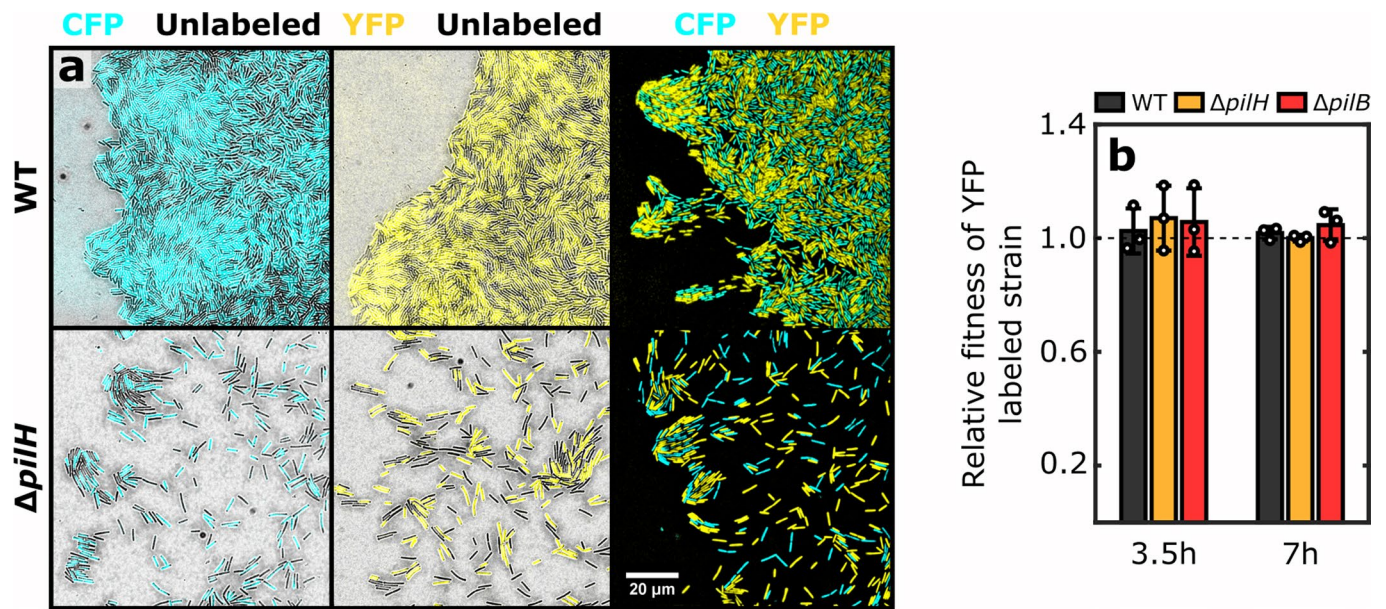
Extended Data Fig. 5 | Rods that propel themselves with larger forces are more likely to become vertically oriented, which disrupts collective movement. **a**, Measurements of the average rod speed as a function of time in three different simulations, each of which contains a uniform population of $N = 1600$ rods with an aspect ratio of $a = 4$ and a self-propulsive force, F . Although rods with $F = 1.5$ collectively move faster than rods with $F = 0.5$, increasing the propulsive force to $F = 3$ causes collective speed to sharply decline over time. **b**, Snapshots of simulations shown in **a** at steady state. Rods are color-coded by their orientation with respect to the surface, ϕ , such that rods lying flat against the surface are shown in red, while those orthogonal to the surface are shown in blue. Rods with larger F are more likely to stand on end, disrupting their capacity to move. **c**, We then performed independent simulations for different values of F and plotted the average rod speed and proportion of rods oriented orthogonal to the surface at steady state (Methods). This shows that the mean speed of the collective peaks at intermediate F , with larger values of F causing rods to become vertically oriented. We denote the force that generates the maximum mean rod speed as F_v . Values of F for simulations shown in **a** and **b** are denoted by coloured arrows. Our results show that out of plane cell rotation places an upper limit on how much propulsive force can be exerted within collectives. Lines and error bars show the mean and standard deviation of three simulations with different (random) initial conditions.



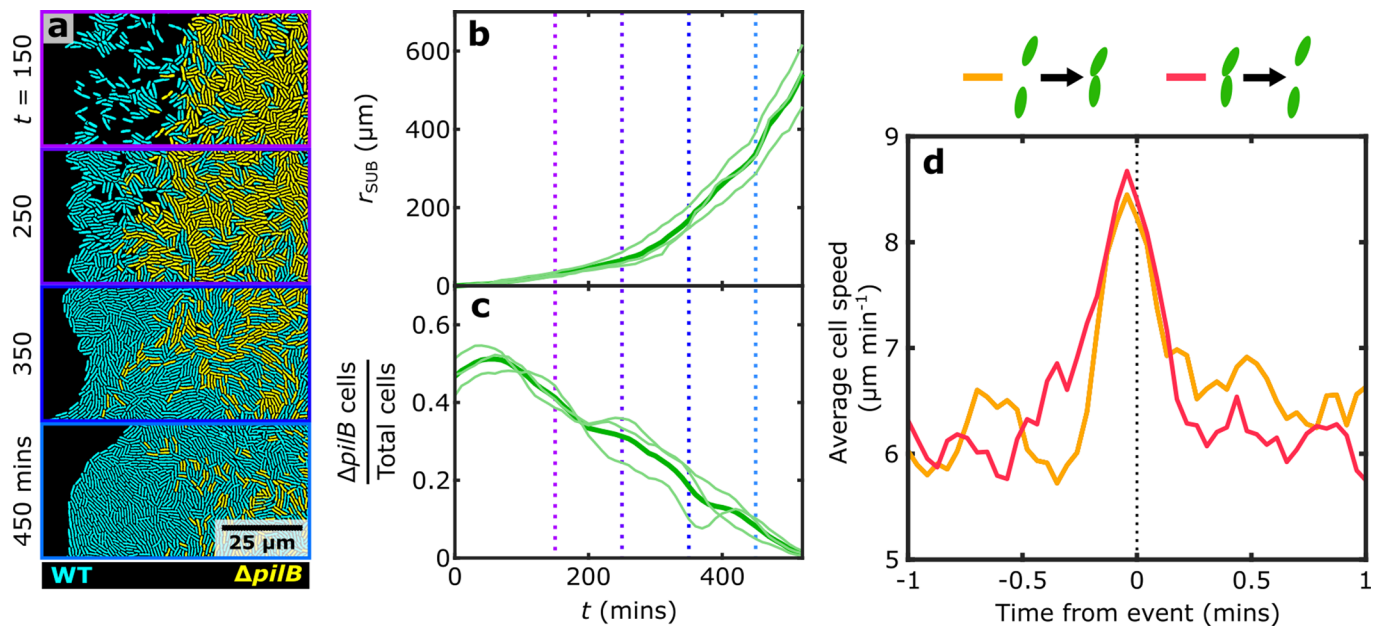
Extended Data Fig. 6 | ΔpilH cells are longer than WT cells, which stabilizes them against verticalization but increases their representation in rosettes when mixed with a shorter genotype. **a**, Boxplots of lengths of WT (black) and ΔpilH (orange) cells mixed together in a high-density subsurface colony ('Monolayer', WT $n = 223$, ΔpilH $n = 218$), a low-density subsurface colony ('Low-density', WT $n = 114$, ΔpilH $n = 84$), and in liquid culture at exponential phase ('Liquid', WT $n = 60$, ΔpilH $n = 34$) (Methods). The ΔpilH cells were significantly longer than WT cells in all three environments (* = $p < 10^{-3}$, ** = $p < 10^{-10}$, Mann-Whitney U test). Boxplots indicate the median (central white rings), interquartile range (box limits), 1.5x interquartile range (whiskers) and outliers (individual circles). **b**, Average rod speed at steady state in 3D SPR monolayer simulations for rods with different propulsive forces, F , and rod aspect ratio, a . All rods in a given simulation have identical parameters. **c**, Proportion of rods oriented vertically at the end of simulations shown in **b**. **d**, Steady-state velocity and verticalization measurements for simulations in which a 'mutant' population of rods that are propelled by a variable force F_2 and with a fixed aspect ratio $a_2 = 5$ interacts with a 'wild-type' population with $F_1 = F_v = 1.5$ (fixed), $a_1 = 4$ (fixed). These simulations are similar to the ones shown in Fig. 4b, except the two populations of rods also have different aspect ratios. Error bars in **b-d** indicate the standard deviation of three separate simulations, each with a different random initial configuration. **e**, A rosette spontaneously generated in co-culture simulation with parameters $F_1 = F_v = 1.5$, $a_1 = 4$, $F_2 = 5$ and $a_2 = 5$ illustrates how the longer length of the mutant enhances its representation in rosettes (compare with Fig. 4c and see Supplementary Notes).



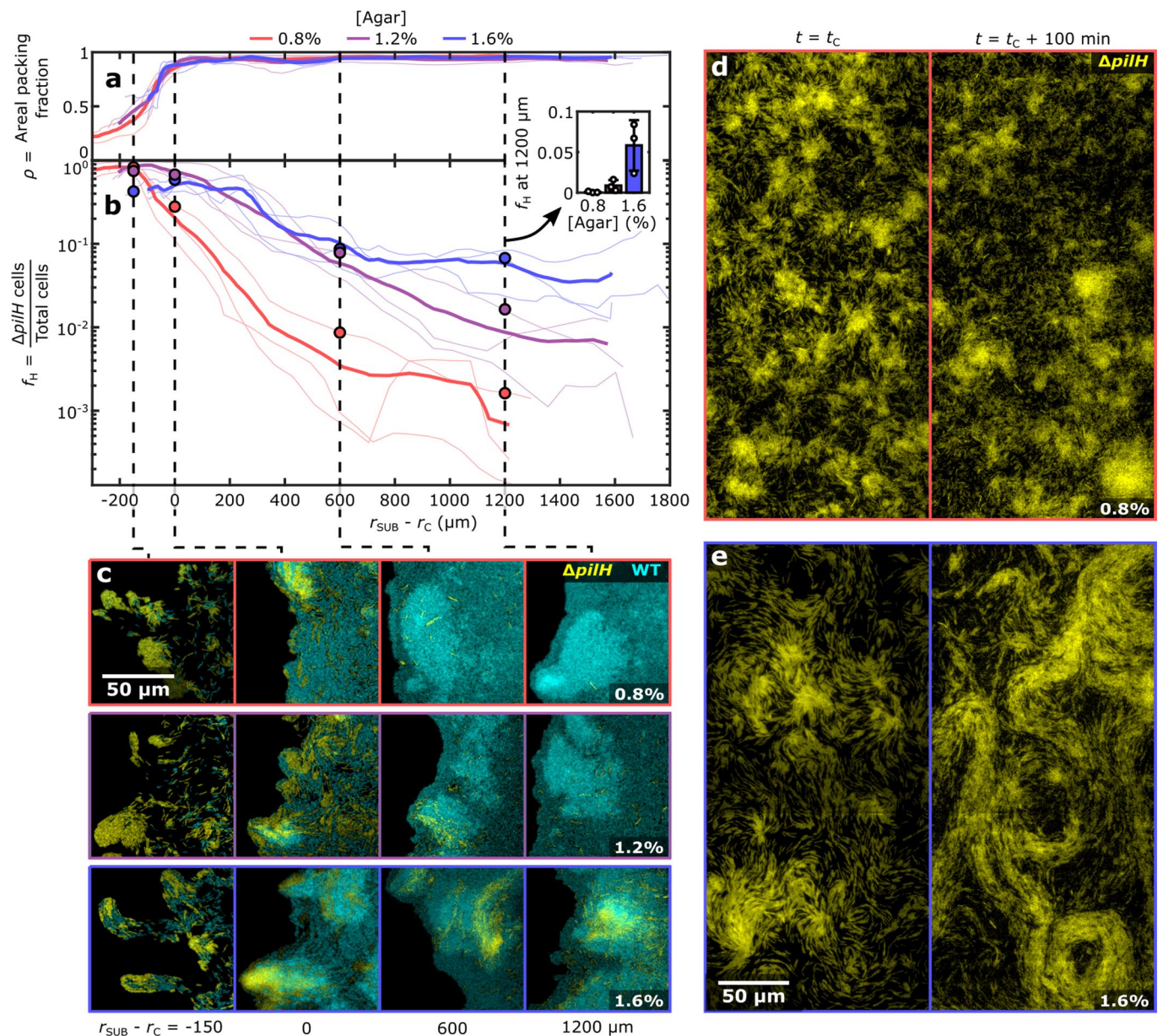
Extended Data Fig. 7 | Rosettes drive convergent flow in a mixed WT/ $\Delta pilH$ subsurface colony and have a topological charge of +1. **a, We used particle image velocimetry (PIV) to quantify collective cell movement in a monolayer of cells over a period of 60 min. The divergence and streamlines of the temporally averaged velocity field reveal that cells locally accumulate (indicated by negative divergence) at rosettes (purple stars). **b**, A timeseries of brightfield images during rosette formation illustrates this process (also shown in Fig. 4d–f and the first part of Supplementary Video 9), with increasing numbers of cells becoming verticalized and trapped within the boundary of the rosette core (white circles) over time. By calculating the director field of these images (Methods), we can calculate the topological charge n around the core of the rosette (**c**, white circular arrows). At all timepoints, the charge of the rosette is equal to +1. In **a**, the region shown in the second part of Supplementary Video 9 is indicated with a white dashed box.**



Extended Data Fig. 8 | Neither labelling cells with constitutively expressed fluorescent proteins nor the deletion of *pilH* or *pilB* has an appreciable impact on the intrinsic growth rate of cells. **a, The leading edge of six different subsurface colonies inoculated with equal fractions of CFP labelled and unlabelled strains (left), YFP labelled and unlabelled strains (middle), and CFP labelled and YFP labelled strains (right) after 16 h of incubation at room temperature. WT and $\Delta pilH$ colonies are shown on the upper and lower rows respectively. In all six colonies, near equal proportions of each cell type are present at the colony's leading edge indicating that expression of a fluorescent label has a negligible impact on each strain's competitive ability. Unlabelled strains are imaged using brightfield and appear grey. **b**, Relative fitness of three YFP labelled test strains (WT, $\Delta pilH$ and $\Delta pilB$) compared to a CFP labelled WT reference strain mixed together in liquid culture. The relative fitness of each test strain was not significantly different from 1 at either 3.5 or 7 h post-inoculation ($p > 0.05$, one sample t-test, $n = 3$, Methods). Error bars indicate standard deviation of 3 replicates.**



Extended Data Fig. 9 | Differences in motility, rather than differences in cell-cell adhesion, drive changes in strain composition at the front of subsurface colonies. **a**, Images of the leading edge of a subsurface colony initialised with equal numbers of $\Delta pilB$ -YFP and WT-CFP cells at 150, 250, 350 and 450 minutes after the start of imaging, processed as shown in Supplementary Fig. 1i. During colony expansion (**b**) a small number of non-piliated $\Delta pilB$ cells were observed to be dragged along by motile WT cells. However, over time the number of $\Delta pilB$ cells near the edge of the colony gradually declined (**c**). These results are in stark contrast to those of equivalent *Neisseria gonorrhoea* colonies, where non-piliated cells are pushed to the colony edge due to decreased intercellular adhesion²⁴. Thick lines in **b** and **c** indicate the mean of three separate colonies. We note that *N. gonorrhoeae* cells are spherical, a shape which is predicted to produce a jammed state in dense collectives¹⁵. In contrast, steric interactions between rod-shaped *P. aeruginosa* cells produce local nematic alignment, which permits collective motility and likely explains why motility is dominant over adhesion in this system. **d**, $\Delta pilH$ cells are hyperpilated, which has been shown to increase cell-cell adhesion in other systems^{24,25}. We tested for the importance of this effect by measuring the mean speed of previously solitary $\Delta pilH$ cells as they came into contact with one another (orange line, $n = 41$) and the mean speed of $\Delta pilH$ cells already in contact with one another as they moved apart (red, $n = 47$). If cells actively adhered to each other, we would expect them to slow down after contacting one another and increase their speed after moving away from one another (Supplementary Notes). We find that cell speed peaks at $t = 0$, which corresponds to the time point at which cells either make or break contact. However, in both cases we observed that there was no appreciable change in cell speed before or after either event, indicating that $\Delta pilH$ cells do not appreciably adhere to each other.



Extended Data Fig. 10 | Stiffer agar suppresses rosettes, increasing the fraction of $\Delta pilH$ cells at the front of mixed WT/ $\Delta pilH$ colonies as they expand.

a, Subsurface colonies prepared with 0.8% (red), 1.2% (purple) and 1.6% (blue) agar were inoculated with equal fractions of WT-CFP and $\Delta pilH$ -YFP cells. Cells in colonies prepared with 1.6% agar are predicted to experience an approximately four-fold larger stabilizing torque compared to those with 0.8% agar, which acts to resist the formation of vertically oriented rosettes (Supplementary Notes). Here, we plot the packing fraction, ρ , at the front of colonies as they expand across the surface, aligning each by the radius at which the front becomes fully packed with cells, or confluent (r_c). This collapses data from all colonies onto a single curve and allows us to control for variation across replicates (Supplementary Notes). **b**, Measurements of the $\Delta pilH$ to total cell fraction, f_H , at the colony front shows that stiffer agar allows $\Delta pilH$ cells to migrate greater distances. The inset shows f_H at $r_{SUB} - r_C = 1200 \mu m$, the final position for which data is available for all replicates. We find that f_H is positively correlated with agar concentration at this position ($p < 0.005$, $n = 9$, Spearman's rank correlation test), demonstrating that stiffer substrates allow $\Delta pilH$ cells to migrate further when competed against WT cells. **c**, The increased persistence of $\Delta pilH$ cells can readily be observed in representative images of the front of 0.8% (top), 1.2% (middle) and 1.6% agar (bottom) colonies. Dashed lines indicate the corresponding positions in **a** and **b**. **d, e**, Images of the region behind the front at the confluency time t_c and $t_c + 100$ min in colonies prepared with 0.8% (**d**) and 1.6% (**e**) agar. With 0.8% agar, $\Delta pilH$ cells form numerous discrete, tightly-packed rosettes. With 1.6% agar, $\Delta pilH$ cells still form aggregations but remain horizontally oriented, allowing them to escape and form plume-like patterns. To improve clarity, only YFP-expressing $\Delta pilH$ cells are shown in **d** and **e**. Thick lines in **a, b** show the mean of three separate colonies.

Reporting Summary

Nature Research wishes to improve the reproducibility of the work that we publish. This form provides structure for consistency and transparency in reporting. For further information on Nature Research policies, see our [Editorial Policies](#) and the [Editorial Policy Checklist](#).

Statistics

For all statistical analyses, confirm that the following items are present in the figure legend, table legend, main text, or Methods section.

- | n/a | Confirmed |
|-------------------------------------|--|
| <input type="checkbox"/> | <input checked="" type="checkbox"/> The exact sample size (n) for each experimental group/condition, given as a discrete number and unit of measurement |
| <input checked="" type="checkbox"/> | <input type="checkbox"/> A statement on whether measurements were taken from distinct samples or whether the same sample was measured repeatedly |
| <input type="checkbox"/> | <input checked="" type="checkbox"/> The statistical test(s) used AND whether they are one- or two-sided
<i>Only common tests should be described solely by name; describe more complex techniques in the Methods section.</i> |
| <input checked="" type="checkbox"/> | <input type="checkbox"/> A description of all covariates tested |
| <input checked="" type="checkbox"/> | <input type="checkbox"/> A description of any assumptions or corrections, such as tests of normality and adjustment for multiple comparisons |
| <input type="checkbox"/> | <input checked="" type="checkbox"/> A full description of the statistical parameters including central tendency (e.g. means) or other basic estimates (e.g. regression coefficient) AND variation (e.g. standard deviation) or associated estimates of uncertainty (e.g. confidence intervals) |
| <input checked="" type="checkbox"/> | <input type="checkbox"/> For null hypothesis testing, the test statistic (e.g. F , t , r) with confidence intervals, effect sizes, degrees of freedom and P value noted
<i>Give P values as exact values whenever suitable.</i> |
| <input checked="" type="checkbox"/> | <input type="checkbox"/> For Bayesian analysis, information on the choice of priors and Markov chain Monte Carlo settings |
| <input checked="" type="checkbox"/> | <input type="checkbox"/> For hierarchical and complex designs, identification of the appropriate level for tests and full reporting of outcomes |
| <input checked="" type="checkbox"/> | <input type="checkbox"/> Estimates of effect sizes (e.g. Cohen's d , Pearson's r), indicating how they were calculated |

Our web collection on [statistics for biologists](#) contains articles on many of the points above.

Software and code

Policy information about [availability of computer code](#)

Data collection

Zen Blue 2012 (Zeiss)
Zen Black 2012 (Zeiss)
NIS-Elements AR v4.51.01 (Nikon)

Data analysis

Commercial software:
Matlab 2018b, including curve fitting and image analysis toolboxes (Mathworks)

Open source software:
ImageJ v1.52n, FIJI distribution (<https://imagej.net/Fiji>)
OrientationJ v2.0.4 (<http://bigwww.epfl.ch/demo/orientation/>)

Custom code:
FAST v0.6 (DOI: 10.5281/zenodo.3630641)
Defector v1.0 (DOI: 10.5281/zenodo.3974873)
colEDGE v1.0 (DOI: 10.5281/zenodo.3974875)

For manuscripts utilizing custom algorithms or software that are central to the research but not yet described in published literature, software must be made available to editors and reviewers. We strongly encourage code deposition in a community repository (e.g. GitHub). See the Nature Research [guidelines for submitting code & software](#) for further information.

Data

Policy information about [availability of data](#)

All manuscripts must include a [data availability statement](#). This statement should provide the following information, where applicable:

- Accession codes, unique identifiers, or web links for publicly available datasets
- A list of figures that have associated raw data
- A description of any restrictions on data availability

Source data for figures 1-4 and extended data figures 1, 3-6, 8-10 are provided with the paper. Additionally, data that support the findings of this study can be accessed at <https://doi.org/10.15131/shef.data.12735251.v1>.

Field-specific reporting

Please select the one below that is the best fit for your research. If you are not sure, read the appropriate sections before making your selection.

- Life sciences Behavioural & social sciences Ecological, evolutionary & environmental sciences

For a reference copy of the document with all sections, see nature.com/documents/nr-reporting-summary-flat.pdf

Life sciences study design

All studies must disclose on these points even when the disclosure is negative.

Sample size	<i>Describe how sample size was determined, detailing any statistical methods used to predetermine sample size OR if no sample-size calculation was performed, describe how sample sizes were chosen and provide a rationale for why these sample sizes are sufficient.</i>
Data exclusions	<i>Describe any data exclusions. If no data were excluded from the analyses, state so OR if data were excluded, describe the exclusions and the rationale behind them, indicating whether exclusion criteria were pre-established.</i>
Replication	<i>Describe the measures taken to verify the reproducibility of the experimental findings. If all attempts at replication were successful, confirm this OR if there are any findings that were not replicated or cannot be reproduced, note this and describe why.</i>
Randomization	<i>Describe how samples/organisms/participants were allocated into experimental groups. If allocation was not random, describe how covariates were controlled OR if this is not relevant to your study, explain why.</i>
Blinding	<i>Describe whether the investigators were blinded to group allocation during data collection and/or analysis. If blinding was not possible, describe why OR explain why blinding was not relevant to your study.</i>

Behavioural & social sciences study design

All studies must disclose on these points even when the disclosure is negative.

Study description	<i>Briefly describe the study type including whether data are quantitative, qualitative, or mixed-methods (e.g. qualitative cross-sectional, quantitative experimental, mixed-methods case study).</i>
Research sample	<i>State the research sample (e.g. Harvard university undergraduates, villagers in rural India) and provide relevant demographic information (e.g. age, sex) and indicate whether the sample is representative. Provide a rationale for the study sample chosen. For studies involving existing datasets, please describe the dataset and source.</i>
Sampling strategy	<i>Describe the sampling procedure (e.g. random, snowball, stratified, convenience). Describe the statistical methods that were used to predetermine sample size OR if no sample-size calculation was performed, describe how sample sizes were chosen and provide a rationale for why these sample sizes are sufficient. For qualitative data, please indicate whether data saturation was considered, and what criteria were used to decide that no further sampling was needed.</i>
Data collection	<i>Provide details about the data collection procedure, including the instruments or devices used to record the data (e.g. pen and paper, computer, eye tracker, video or audio equipment) whether anyone was present besides the participant(s) and the researcher, and whether the researcher was blind to experimental condition and/or the study hypothesis during data collection.</i>
Timing	<i>Indicate the start and stop dates of data collection. If there is a gap between collection periods, state the dates for each sample cohort.</i>
Data exclusions	<i>If no data were excluded from the analyses, state so OR if data were excluded, provide the exact number of exclusions and the rationale behind them, indicating whether exclusion criteria were pre-established.</i>
Non-participation	<i>State how many participants dropped out/declined participation and the reason(s) given OR provide response rate OR state that no participants dropped out/declined participation.</i>

Randomization

If participants were not allocated into experimental groups, state so OR describe how participants were allocated to groups, and if allocation was not random, describe how covariates were controlled.

Ecological, evolutionary & environmental sciences study design

All studies must disclose on these points even when the disclosure is negative.

Study description

Briefly describe the study. For quantitative data include treatment factors and interactions, design structure (e.g. factorial, nested, hierarchical), nature and number of experimental units and replicates.

Research sample

Describe the research sample (e.g. a group of tagged *Passer domesticus*, all *Stenocereus thurberi* within Organ Pipe Cactus National Monument), and provide a rationale for the sample choice. When relevant, describe the organism taxa, source, sex, age range and any manipulations. State what population the sample is meant to represent when applicable. For studies involving existing datasets, describe the data and its source.

Sampling strategy

Note the sampling procedure. Describe the statistical methods that were used to predetermine sample size OR if no sample-size calculation was performed, describe how sample sizes were chosen and provide a rationale for why these sample sizes are sufficient.

Data collection

Describe the data collection procedure, including who recorded the data and how.

Timing and spatial scale

Indicate the start and stop dates of data collection, noting the frequency and periodicity of sampling and providing a rationale for these choices. If there is a gap between collection periods, state the dates for each sample cohort. Specify the spatial scale from which the data are taken

Data exclusions

If no data were excluded from the analyses, state so OR if data were excluded, describe the exclusions and the rationale behind them, indicating whether exclusion criteria were pre-established.

Reproducibility

Describe the measures taken to verify the reproducibility of experimental findings. For each experiment, note whether any attempts to repeat the experiment failed OR state that all attempts to repeat the experiment were successful.

Randomization

Describe how samples/organisms/participants were allocated into groups. If allocation was not random, describe how covariates were controlled. If this is not relevant to your study, explain why.

Blinding

Describe the extent of blinding used during data acquisition and analysis. If blinding was not possible, describe why OR explain why blinding was not relevant to your study.

Did the study involve field work? Yes No

Field work, collection and transport

Field conditions

Describe the study conditions for field work, providing relevant parameters (e.g. temperature, rainfall).

Location

State the location of the sampling or experiment, providing relevant parameters (e.g. latitude and longitude, elevation, water depth).

Access & import/export

Describe the efforts you have made to access habitats and to collect and import/export your samples in a responsible manner and in compliance with local, national and international laws, noting any permits that were obtained (give the name of the issuing authority, the date of issue, and any identifying information).

Disturbance

Describe any disturbance caused by the study and how it was minimized.

Reporting for specific materials, systems and methods

We require information from authors about some types of materials, experimental systems and methods used in many studies. Here, indicate whether each material, system or method listed is relevant to your study. If you are not sure if a list item applies to your research, read the appropriate section before selecting a response.

Materials & experimental systems

n/a	Involvement in the study
<input checked="" type="checkbox"/>	<input type="checkbox"/> Antibodies
<input checked="" type="checkbox"/>	<input type="checkbox"/> Eukaryotic cell lines
<input checked="" type="checkbox"/>	<input type="checkbox"/> Palaeontology and archaeology
<input checked="" type="checkbox"/>	<input type="checkbox"/> Animals and other organisms
<input checked="" type="checkbox"/>	<input type="checkbox"/> Human research participants
<input checked="" type="checkbox"/>	<input type="checkbox"/> Clinical data
<input checked="" type="checkbox"/>	<input type="checkbox"/> Dual use research of concern

Methods

n/a	Involvement in the study
<input checked="" type="checkbox"/>	<input type="checkbox"/> ChIP-seq
<input checked="" type="checkbox"/>	<input type="checkbox"/> Flow cytometry
<input checked="" type="checkbox"/>	<input type="checkbox"/> MRI-based neuroimaging